Resistivity of Endotaxial Silicide Nanowires

Measured with a Scanning Tunneling Microscope

by

Samuel Tobler

A Dissertation Presented in Partial Fulfillment
Of the Requirements for the Degree
Doctor of Philosophy

Approved July 2011 by the
Graduate Supervisory Committee:

Peter Bennett, Chair
Martha McCartney
Nongjian Tao
Bruce Doak
Tingyong Chen

ARIZONA STATE UNIVERSITY

December 2011

ABSTRACT

In this project, a novel method is presented for measuring the resistivity of nanoscale metallic conductors (nanowires) using a variable-spacing 2-point method with a modified ultrahigh vacuum scanning tunneling microscope. An auxiliary field emission imaging method that allows for scanning insulating surfaces using a large gap distance (20nm) is also presented. Using these methods, the resistivity of self-assembled endotaxial $FeSi_2$ nanowires (NWs) on Si(110) was measured. The resistivity was found to vary inversely with NW width, being ρ_{NW} = 200 μΩ cm at 12 nm and 300 μΩ cm at 2 nm. The increase at small w is attributed to boundary scattering, and is fit to the Fuchs-Sondheimer model, yielding values of ρ_0 = 150 μΩ cm and λ = 2.4 nm, for specularity parameter p = 0.5. These results are attributed to a high concentration of point defects in the $FeSi_2$ structure, with a correspondingly short inelastic electron scattering length. It is remarkable that the defect concentration persists in very small structures, and is not changed by surface oxidation.

ACKNOWLEDGEMENTS

This work has been long and hard. I would not have gotten to the end without the help of many different people. I first want to thank my advisor, Peter Bennett, for his guidance and direction in the years we have known each other. He has taught me what is important in research and how to properly conduct an experiment.

I need to thank the faculty members who have been on my committee, Martha McCartney, Bruce Doak, Nongjian Tao, Jeff Drucker, and Tingyong Chen, for helping when I needed help and giving me encouragement to the end.

Next, I want to thank those who I have shared lab space, Dr. Lifeng Hao, Travis Bain, Jingyi Huang, Adam Blake, Devon Powell, and Hyungwoo Choi for providing useful feedback and companionship in the lab.

Lastly, I want to thank my wife and kids for being patient with me for my long hours in the lab and for their love toward me throughout this experience.

TABLE OF CONTENTS

Page

LIST OF FIGURES viii

LIST OF TABLES xvi

CHAPTER

1 INTRODUCTION 1

2 RESISTIVITY OF METALS 3

2.1 Drude Model 3

2.2 Sommerfeld model 5

2.3 Boundary Scattering 6

2.4 Grain Boundary Scattering 8

3 BACKGROUND ON SILICIDE NANOWIRE STRUCTURE AND GROWTH 13

3.1 Silicides 13

3.2 Rare Earth Nanowires 14

3.3 Endotaxial NWs 17

4 MEASURING RESISTIVITY 22

CHAPTER Page

4.1 Contact Resistance 22

4.2 4-Point Method 22

4.3 2-Point Variable-Distance Method 24

4.4 Ex Situ Resistivity Measurements 25

4.5 Multi Probe STM Instrument 26

5 INSTRUMENTATION AND SAMPLE PREPARATION METHODS 29

5.1 STM 29

5.2 Tip Preparation 31

5.3 Contact Pad 38

5.4 Sample Preparation Chamber 42

5.5 Sample Fabrication 46

5.6 Controlled Approach to Contact 48

6 SCANNING FIELD EMISSION IMAGING 55

6.1 Field Emission Process 55

6.2 Lateral Resolution and Analytic Model 58

CHAPTER Page

6.3 Field Emission Scanning 59

6.4 Bias Curve: Analytic Model 61

6.5 Bias Curve: Numeric Model 61

6.6 Noise 67

6.7 Images of Oxidized Silicon 67

7 PLATINUM / SILICON (100) NANOWIRES: GROWTH 71

7.1 Introduction 71

7.2 PtSi Nanowires 71

8 IRON / SILICON (110) NANOWIRES: RESISTIVITY 75

8.1 Iron Silicide Compounds 75

8.2 Nanowires 75

8.3 Determination of Cross Sectional Area 76

8.4 Resistance vs Distance Data 79

8.5 ρ vs Size Data 81

8.6 Temperature and Surface Oxide Effects 83

CHAPTER Page

9 SUMMARY AND FUTURE WORK 87

BIBLIOGRAPHY 90

LIST OF FIGURES

Page

2. 1. Conducting material of length, L, and width, d, showing electron paths for scattering from phonons, the top surface boundary, and a grain boundary. ... 7

2. 2. (a) Cross section and (b) top view TEM images of a copper filled trench used for measurements. (c) Measured resistivity of thin Cu wires at room temperature (circular symbols) with combined model (solid line), MS model (dot-dash line), FS model (dashed line) and bulk Cu value (dotted line). (after Steinhogl *et al*) [17] 10

2. 3. $CoSi_2$/Si (110). Inset is cross section TEM shows single crystal endotaxial structure. (after Zhe – PhD thesis) 11

3. 1. Schematic showing the making of $CoSi_2$ by reactive deposition. Co atoms arrive on a heated Si surface. They combine with Si adatoms that are thermally excited from the step edges.. 14

3. 2. (a) SEM image showing an epitaxial triangular silicide (labeled A) and an endotaxial silicide NW (labeled B) on Si (111). Cross section TEM images of (b) NW and (c) triangular structure. (after He *et al*) [19]........................ 15

3. 3. (a) DySi2 NWs on Si (100) [20]. (after Preinesberger *et al*) (b) Model of how asymmetric strain can cause the NW shape. Silicide structure dimension a matches Si spacing while dimension c is about 10% different. The strain along c limits growth while along a it does not, so the NW is elongated in this direction.. 16

Figure Page

3. 4. (a) NW with different growth rates for length and width. CoSi2 NWs on Si (110) grown at (b) 780°C and (c) 700°C with cross-section TEM (c inset). (after He *et al*) [19] 19

3. 5. The Si steps (solid lines) flow in or out to accommodate the growth of NWs. NW end B is forcing a step to retreat. NW end A is forcing the step to advance. Dotted lines are impurities on the surface..................................... 20

4. 1. 4-point measuring technique for NW resistivity. Each contact has a contact resistance. A known current is passed through the outer two contacts and voltage is measured on the inner two. The NW is separated from the Si substrate by a Schottky barrier which behaves as a diode. 23

4. 2. SEM image of contacts on a NW. The contacts were added ex situ (after growth of the NWs in UHV) by electron beam lithography......................... 25

4. 3. SEM image of Prof Hasegawa's multi-probe STM being used as a 4-point probe to measure the resistivity of a $CoSi_2$ NW on Si (110). The inner two contacts can also be used in a 2-point variable-spacing configuration. Comparison between the 4-point and "hot" 2-point resistance yielded R_{4pt}=207Ω and R_{2pt}=237Ω resulting in Rc=30Ω. [43] (after Okino *et al*).... 26

4. 4. (a) SEM of Professor Hasegawa's multi-probe STM being used as a 2-pt variable distance probe on 30 nm wide CoSi2 NWs on Si (110). Measurements were taken at T=300K. (b) Resistance vs probe spacing data. [43] (after Okino *et al*) 27

Figure Page

4. 5. SEM image of Professor Hasegawa's multi-probe STM being used as a 4-point probe to measure the resistivity of a $CoSi_2$ NW. The tips have PtIr coated carbon naotubes (CNT) ends. [44] (after Yoshimoto *et al*)............... 28

5. 1. RHK UHV 300 [46]... 30

5. 2. (a) Image of 'Beetle' type STM. Tip hangs above sample. Legs walk down incline to bring tip to sample. (b) Top view of STM sample holder showing electrical contacts sticking out on left. The sapphire ring has inner diameter of 5mm. 31

5. 3. Schematic of tip etching by first method. This current flows from W wire through KOH solution to submerged electrode. Etching occurs on surface of solution to form a decaying neck. After the neck breaks the top is used for STM tip and the bottom is discarded. 32

5. 4. Current vs time during etching of tip. At around 800 seconds the neck breaks and the etching is quickly turned off... 33

5. 5. Optical image of W wire etched with first etching method. Inset is a closer view of the tip. 34

5. 6. Schematic of tip etching by second method. The current passes from W wire though the KOH film to the other electrode. The etched neck forms in film. After the neck breaks the lower portion falls into shaving cream and is used as STM tip. The upper portion is not used as STM tip. 35

5. 7. SEM image of tip etched with second method. 36

Figure Page

5. 8. Current setup for STM etching. The W wire and Ni loop holding KOH film are held by magnets for ease of alignment. The shaving cream below will catch fallen tip after etched neck breaks. 37

5. 9. (a) Tip attached to Ta heater bar for annealing. Tip faces down toward anode for field emission check of tip sharpness. (b) The schematic of annealing process and field emission process. All done in turbo system at 10^{-6} Torr... 38

5. 10. V_{FET} vs tip radius R for I=20nA.. 39

5. 11. Schematic displaying dimensions during contact pad deposition. Filament is a 0.5 mm thick linear source orientated parallel to the mask – sample interface 2.5 cm away. The mask sits 1 μm above the sample. Geometrically, the pad edge can be 20 nm. The inset displays color image without values. 40

5. 12. SEM image verifying mask – sample interface. Inset is enlarged interface showing gap size of 1 μm between mask and sample................................. 41

5. 13. Contact pad edges made from (a) Au, (b) Pt, (c) Co, and (d) Ti. 43

5. 14. Sample prep chamber. The STM sample holder sits on center column. Within the column is a heater filament. The copper fork on left attaches to the sample holder's electrical contacts. The larger Mo mask protects sample holder. The Ti linear filament is located at the top right of image. 45

5. 15. Schematic of fabricated sample: (a) top, (b) side. First, Ta is deposited to form 50 nm thick pads on side. Second, NWs are made. Third, the contact pad is deposited to connect NWs to $TaSi_2$ pad. STM tip connects with NW to complete circuit shown in (c).. 47

Figure Page

5. 16. SEM images of carbon nanotube on end of W etched tip (a) before contacts and (b) after over 100 contacts with sample. CNT still at end of tip. 49

5. 17. Current vs z with CNT tip. Inset is an image scanned by a tip after repeated contact with the surface showing atomic resolution is still possible. 50

5. 18. Current vs z with W etched tip. The inset is a scanned image after the repeated gentle contacts displaying the atomic resolution is still possible... 51

5. 19. Front Panel of the LabView VI constructed to follow I vs z during tip approach and capture R(x,y,z) measurements. 53

5. 20. Block diagram of the VI from Figure 5.18. 54

6. 1. (a) Band diagram and (b) field map for STM operation under normal conditions (g=0.5nm, Vb=1V, I=1nA, and g<R). (c) Band diagram and (d) field map for STM operation under field emission conditions (g>R and V>Φ). 56

6. 2. Gap spacing vs V_{bias} for $+V_{bias}$ and $–V_{bias}$. Analytic fits to the data are shown as solid lines with the measured data as the symbols x and * for $+V_{bias}$ and $–V_{bias}$ respectively. 60

6. 3. Gap spacing vs V_{bias} for $+V_{bias}$ and $–V_{bias}$. The numerical fits to the data are shown as connected lines with the measured data as squares and triangles for $+V_{bias}$ and $–V_{bias}$ respectively. 62

6. 4. Contour map of potential V(r,z) in cylindrical coordinates with V_{tip} = 1 (conical shape) and V_{sample} = 0 (at z = 0). 64

Figure Page

6. 5. The SFE images of steps on Si (111) for V_{bias} equals (a) +1V, (b) +10V, (c) +20V, (d) +30V, (e) +40V, and (f) +50V. The same area is imaged for (b)-(f). 65

6. 6. The SFE images of steps on Si (111) for V_{bias} equals (a) -1V, (b) -10V, (c) -20V, (d) -40V, (e) -50V, and (f) -100V. The same area is imaged for (b)-(f). 66

6. 7. The line scans over a step for field emission images for (a) $+V_{bias}$ and (b) $-V_{bias}$. The higher V_{bias} line scans are offset for easier comparison. The lower lateral resolution is evident in the larger V_{bias} line scans by the broadening of the atomic step. 68

6. 8. Noise plots for V_{bias} = -50V and +50V. (a) Line scan of the 'noise' image. For $+V_{bias}$ the step-jump occurs twice within the 25ms. The $-V_{bias}$ noise levels are mainly the 60 Hz harmonic oscillations. (b) Frequency vs log(Signal) for both $+V_{bias}$ and $-V_{bias}$. $+V_{bias}$ noise is 100 times larger for $f < 100$ Hz. 69

6. 9. The SFE images of the atomic steps under oxide with thicknesses of (a) 2.3 nm and (b) 3.1 nm on Si (111). V_{bias} = -10 V. 70

6. 10. SFE images $CoSi_2$ NWs on Si (110) after sample sat in air for 1 month. V_{bias} = -10V. 70

Figure Page

7. 1. AFM images of PtSi nanowires on Si (100) (a) 600°C, (b) 700°C, (c) 750°C, and (d) 800°C growth temperatures. The NWs grow progressively larger and less dense with the increasing T. 72

8. 1. (a) $FeSi_2$ NWs on Si (110). Cross-section TEM image (inset) displaying bunched Si around NW. There are linescans overlapped in (b) also displaying Si steps bunching together around NW. The width of NW convoluted from STM tip. 76

8. 2. (a)-(f) Cross section TEM images of $FeSi_2$ NWs on Si (110). Scale in (e) is used for all images. (g) Height above surface vs Area as determined by (a)-(f) with corresponding fit curve. 77

8. 3. (a) Three NWs laying across (NW1), under (NW2), and away (NW3) from Ti contact pad, displayed as a dotted line. (b) NW1 after many contacts for measurements displaying minimal damage. (c) Linescan on NW1 displaying height above bunched Si. (d) R vs L curve along NW1 with R vs L parallel to NW1 for contact pad formation (inset). 80

8. 4. ρ vs $\sqrt{A}$ for 22 NWs on 3 samples ranging T = 700 – 800°C. Two Fuchs – Sondheimer fits are shown for p = 0.5 (solid line) and 0 (dashed line) and ρ_0 = 150 μΩ cm. λ values are found to be 5 and 2.4 nm respectively. 82

8. 5. (a) R(L) curve for NW measured at T = 300K and 130K. dR/dL = 1.80 ± 0.1 kΩ/nm and 1.3 ± 0.3 kΩ/nm respectively (b) R(L) curve for air exposed NW. ρ = 280 ± 100 μΩ cm for $\sqrt{A}$ = 3.2 nm. 85

Figure Page

9. 1. Plot of various NWs by $\sqrt{A}$ vs ρ on the same axis. Includes all values currently published. $FeSi_2$ NWs studied in this project added as red star. ... 88

LIST OF TABLES

PAGE

3. 1 List of all currently known endotaxial silicide NW systems. 21

5. 1. Results of contact pad edges from Au, Pt, Co, and Ti. The stability column tells if film stays low resistive for long periods of time (> 1 day). 44

7. 1. PtSi NWs on Si (100) at various T in UHV. 74

9. 1. Measured resistivity values for various metallic NWs as found in current publications. All values given at 300K. FeSi2 NWs studied in this project are added at bottom. 89

INTRODUCTION

Silicide structures are important in many different applications. They are used as ohmic contacts,[1] gate electrodes, [2] local interconnects, [3] Schottky barrier contacts, [4-7] and diffusion barriers. [8] Electronic devices are becoming smaller every year. An understanding of the electrical behavior of silicide materials on the nanoscale is needed to continue the development of improved devices.

This work will show an in-depth study of silicide nanowires (NWs). An understanding of how current flows through metal is discussed. Also included is a simplified model for the nature of metals.

Resistivity within NWs is desired. This project discusses the techniques used to measure resistivity. Among these are multi-tip STM and electron beam lithography. For this work a single tip STM and contact pad are used in a 2-point variable spacing method.

Designing, building and implementing the tools needed to perform the measurements will be shown and explained. Specifically, a sample preparation chamber was built for the purpose of fabricating the samples in UHV. STM tip preparation and sharpness measurements will also be discussed.

A new method for imaging large features with field emission is shown. A simple analytical and numerical model is fit to the data of tip-sample gap vs bias voltage. It is shown that field emission scanning is safer for the STM tip without damaging the sample.

NWs made from platinum deposited on silicon (100) are imaged with STM and AFM.

Lastly, this dissertation will explore $FeSi_2$ NWs on Si (110). Resistance vs probe separation curves are analyzed to find NW resistivity. An in depth explanation for determining calculated resistivity, ρ, values is given. STM and TEM images are used to determine the cross section of NWs. A connection to small conductor models is made.

This work will help further the understanding of conductors on the nanoscale. This work will help others determine the feasibility in using these NWs in future technology.

2

RESISTIVITY OF METALS

2.1 Drude Model

In this dissertation, we concern ourselves with understanding how resistivity behaves in nanoscale conductors. As electronic devices become smaller and the metal interconnects are correspondingly smaller, we desire to understand how these structures behave on the small scale. Specifically we have studied long, thin conductors, which are sometimes called “nanowires” (NWs). [9] We are concerned only with diffusive charge transport, not ballistic or quantum transport. The latter topics pertain to structures that are smaller and/or semiconducting. In this instance we are concerned with metallic structures with dimensions larger than $1/k_F$.

We begin by considering the Drude model of electron conduction in metals. [10] In this model, a metal is treated as a lattice of immobile ions with electrons flowing around them. The electrons are treated as non-interacting, except for random collisions with lattice defects; so in the absence of an external electric field, they will move in straight lines between collisions. The mean time between collisions is taken as τ, the relaxation time, such that in a time interval dt the probability of the electron undergoing a collision is dt/τ.

A collection of n electrons flowing with drift velocity $\mathbf{v_d}$ corresponds to a current density

$$\mathbf{j} = -ne\mathbf{v}\,, \qquad \text{(Eq. 2.1)}$$

with n being the electron density, e is the charge of an electron, and

$$\mathbf{v} = \mathbf{v}_0 + \mathbf{v}_d, \qquad \text{(Eq. 2.2)}$$

where $\mathbf{v_0}$ is the initial velocity immediately after a collision and $\mathbf{v}_d$, drift velocity, is the added velocity achieved by forces acting on the electron for a time t. The drift velocity is defined as $\mathbf{v}_d = -e\mathbf{E}t/m$, where **E** is the electric field, t is the time of flight between collisions, and m is the mass of the electron. The electrons are assumed to move in random directions after a collision so $\mathbf{v}_0$ is random and does not contribute to the overall velocity, **v**. Therefore, **v** must be made up entirely by $\mathbf{v}_d$. Putting $\mathbf{v}_d$ into Eq 2.1, we have

$$\mathbf{j} = \left(\frac{ne^2\tau}{m}\right)\mathbf{E}, \qquad \text{(Eq. 2.3)}$$

where τ is placed in the equation instead of t for the average of the time of flight. Eq. 2.3 defines a linear vector relationship, which comprises Ohm's law:

$$\mathbf{j} = \sigma\mathbf{E} \text{ (Amps/m}^2\text{)}, \qquad \text{(Eq. 2.4)}$$

where σ is the conductivity of the material. The Drude expression for resistivity, ρ, then is given by

$$\rho = \frac{1}{\sigma} = \frac{m}{ne^2\tau} \; (\Omega \text{ m}). \qquad \text{(Eq. 2.5)}$$

For a pair of contacts, with total current flow I and voltage drop V, we can define a resistance of R =V/I. For one dimensional uniform current flow, as is the case for our NWs, the resistance is given as,

$$R = \frac{\rho L}{A}, \qquad \text{(Eq. 2.6)}$$

where L is the distance between contacts and A is the cross sectional area of the material.

2.2 Sommerfeld model

It is useful to develop the notion of mean free path between collisions. This requires a more thorough analysis of the electron velocity. By treating the electrons as quantum particles in a box with periodic boundary conditions, we can solve their wave function which satisfies the Schrodinger equation. This gives a solution of

$$\psi_k(\mathbf{r}) = \frac{1}{\sqrt{V}} e^{i\mathbf{k}\bullet\mathbf{r}} \qquad \text{(Eq. 2.7)}$$

where ψ_k is normalized to give a probability of 1 for finding the electron somewhere in a box of size V. Under these conditions, the electron energy is given by

$$E(\mathbf{k}) = \frac{\hbar^2 k^2}{2m}, \qquad \text{(Eq. 2.8)}$$

where **k** is the wave vector. Applying the periodic boundary condition gives a collection of wave vectors that form a basis for k-space. Each position is distanced from its nearest neighbors by $2\pi/L$ and occupies a space $(2\pi/L)^3 = 8\pi^3/V$.

As electrons are fermions, no two can occupy the same spatial state. Accounting for the electron spin = ½, we fill up the k-space starting with the lowest energy, the origin in k-space. After this we work outward until all the electrons are accounted for. For large N, the occupied k-space is a sphere of

radius k_f, where k_f is the Fermi wave vector. This treatment assumes T=0, however, variations at room temperature cause only small deviations.

N is determined from

$$N = \left(\frac{4\pi k_f^3}{3} \right) 2 \left(\frac{V}{8\pi^3} \right) = \frac{k_f^3}{3\pi^2} V \ , \qquad \text{(Eq. 2.9)}$$

where the number 2 accounts for the two spin states for electrons. This now gives an electron density of

$$n = \left(\frac{N}{V} \right) = \frac{k_f^3}{3\pi^2} \ . \qquad \text{(Eq. 2.10)}$$

Plugging this quantity back into Eq 2.5 with the additional information of $\tau = \lambda/v$, where λ is the mean free path of the electrons, and momentum, $\mathbf{p} = \hbar\mathbf{k} = m\mathbf{v}$, and rearranging terms we get

$$\rho(T)\lambda(T) = \frac{3\pi^2\hbar^2}{e^2 k_f^2} \ . \qquad \text{(Eq. 2.11)}$$

Eq 2.11 allows us to estimate λ from a measured value for ρ. This is the Sommerfeld model of conduction in metals.

2.3 Boundary Scattering

The Drude model does not consider boundaries of the materials. Our NWs have widths that can be similar in size to λ, as seen in Figure 2.1. In this example, we have $d > \lambda$ by a small amount. The electrons will therefore interact with the boundaries. We must account for any effects caused by this interaction. It is useful to separate this effect in our study of resistivity in NWs.

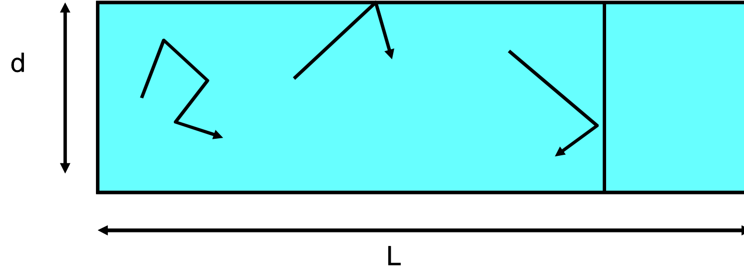

FIG. 2. 1. Conducting material of length, L, and width, d, showing electron paths for scattering from phonons, the top surface boundary, and a grain boundary.

Boundary scattering[11] plays an important role in the resistivity of NWs. Roughly speaking, electrons within a distance λ from the boundary have a significant probability of interacting with the boundary. The central arrow in Figure 2.1 shows an inelastic scattering that can result from this interaction.

Fuchs and Sondheimer (F-S) developed an expression for boundary scattering effects on resistivity for a round conductor. [12] Later, other shapes were considered by other workers. F-S provided a statistical evaluation of interaction with the boundary. The model relates the increase in resistivity of the material to the type of collision at the boundary; whether it is elastic with no effect on $\mathbf{v}_d$ or inelastic, which reduces the drift velocity. The F-S model may be written, approximately, as:

$$\rho_{FS} / \rho_0 \approx 1 + \frac{3}{4}(1-p)\frac{\lambda}{d}, \qquad \text{(Eq. 2.12)}$$

where ρ_0 is the bulk resistivity of the material, p is the fraction of electrons specularly scattered at the boundary, and d is the diameter of the wire. This

expression is intended as a perturbation with the condition $\frac{d}{\lambda} >> 1$, however it is widely used [13-15]with d/λ < 1, as in our experiment.

2.4 Grain Boundary Scattering

An additional resistance may occur in narrow conductors due to internal scattering. This generally refers to grain boundaries within the material. These grain boundaries are an extended defect in the material that causes additional scattering of the electrons. Fabricated NWs, like copper interconnects, have a polycrystalline structure. They are made of many different crystallographic grains whose boundaries will interact with the flowing electrons. Figure 2.1 shows this interaction on the right side of the image. As the material shrinks to the nanoscale, the grains that make up the wire may be comparable in size to λ.

A model was developed to describe the contribution to resistivity from grain boundaries. This was done by A. F. Mayada and M. Shatzkes in 1969. [16] They took the theory from Fuchs and Sondheimer and expanded the concepts to include the effects of grain boundary scattering. This additional term is:

$$\rho_{MS} / \rho_0 = \left[1 - \frac{3\alpha}{2} + 3\alpha^2 - 3\alpha^3 \ln\left(1 + \frac{1}{\alpha}\right)\right]^{-1}, \qquad \text{(Eq. 2.13)}$$

where

$$\alpha = \frac{\lambda}{d}\left(\frac{R}{1-R}\right) \qquad \text{(Eq. 2.14)}$$

and R is the reflectivity coefficient of the grain boundary and the other symbols are the same as those in the F-S equation. Since the internal boundaries are not parallel to the current flow, specular reflections will alter the momentum along **E**.

The effects of these two mechanisms can be combined using Matthiessen's rule, which states that scattering rates add for statistically independent events. Thus,

$$\frac{1}{\tau} = \frac{1}{\tau_{FS}} + \frac{1}{\tau_{MS}} + \frac{1}{\tau_{bg}}, \qquad \text{(Eq. 2.15)}$$

where τ_{bg} is the diffusive background scattering.

Steinhogl et al applied these models to copper lines formed with the Damascene process. Damascene copper is currently used for interconnects in silicon microelectronic devices. This process creates trenches for the desired interconnect. Copper is added to the point of overflowing the trenches. A polishing process removes any copper above the insulating layer. This leaves the trenches filled with copper to provide the interconnection desired.

Figures 2.2a and 2.2b show the top view and cross section respectively of typical copper interconnects. [17] As can be seen in this figure, the copper lines contain many internal grains. The narrowest lines that were obtainable were 40 nm. Bulk copper, of high quality, has $\rho = 2.0\ \mu\Omega$ cm at T = 300 K. From Eq. 2.11 we infer $\lambda \sim 40$ nm. The scattering in copper at 300K is almost entirely from phonons. In Figure 2.2c, experimental data for the resistivity of the copper lines is plotted against the line width. Steinhogl also showed the curves from the F-S model and the Mayadas-Shatzkes model. When the two models are combined by

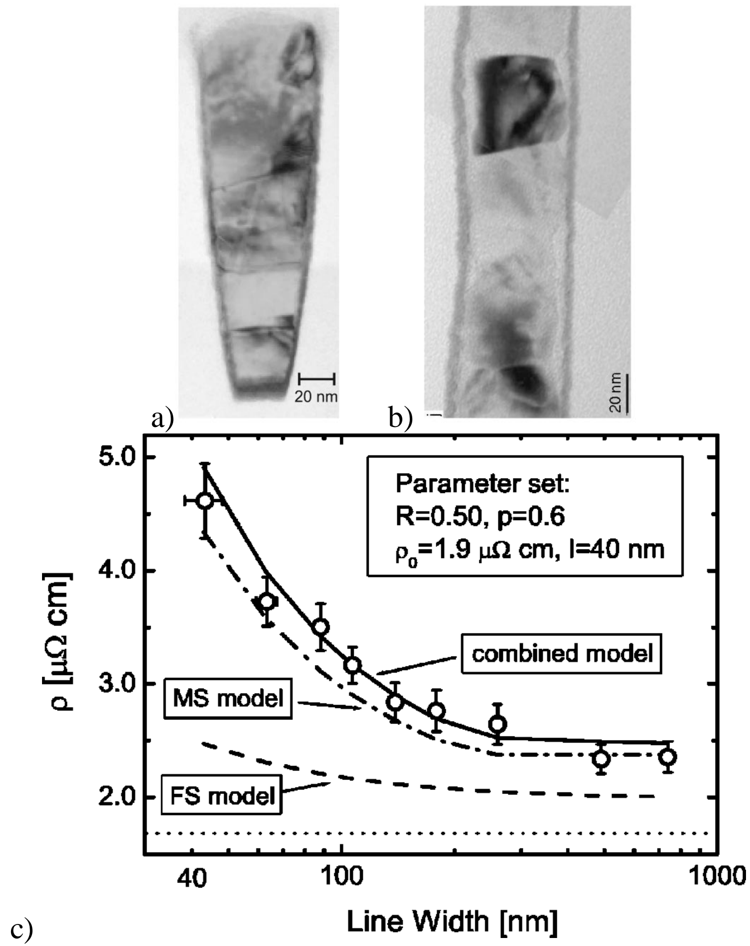

FIG. 2. 2. (a) Cross section and (b) top view TEM images of a copper filled trench used for measurements. (c) Measured resistivity of thin Cu wires at room temperature (circular symbols) with combined model (solid line), MS model (dot-dash line), FS model (dashed line) and bulk Cu value (dotted line). (after Steinhogl *et al*) [17]

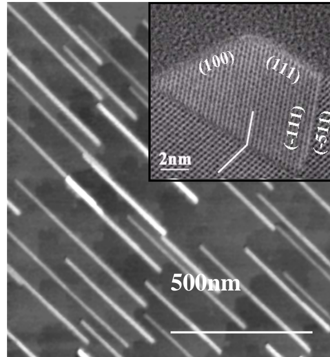

FIG. 2. 3. $CoSi_2$/Si (110). Inset is cross section TEM shows single crystal endotaxial structure. (after Zhe – PhD thesis)

Matthiessen's rule, the model agrees with experimental values with parameters reflectivity R = 0.50 and specular fraction p = 0.6.

The endotaxial NWs discussed in this dissertation are different from the Damascene lines studied by Steinhogl. They are much smaller in width (as low as 2nm). Also, the NWs are single crystal, as described later, and shown in Figure 2.3. Figure 2.3 shows $CoSi_2$ NW on Si (110). The inset is a cross section TEM image that shows the perfect crystal structure. The single crystal structure of the NWs corresponds to $\alpha \to 0$ in the Mayadas-Shatzkes equation, or no grain boundaries to reflect the electrons.

Additionally, the boundaries of the NWs are nearly perfect in structure; therefore, electrons are expected to have elastic collisions at the boundaries. This has been found to be the case for epitaxial silicide layers. [18] This corresponds to p = 1 in the F-S equation. One can therefore anticipate that the resistivity of self-assembled silicide NWs will show little or no size effect. In this sense, very small endotaxial NWs could be "better than copper."

The scale of the F-S model predicts $\rho \sim 1/d$. This means ρ will be very large for $d \sim 2$ nm. The Damascene process cannot make copper lines on this scale, but our NWs do reach this. This provides motivation for this study.

3

BACKGROUND ON SILICIDE NANOWIRE STRUCTURE AND GROWTH

3.1 Silicides

Metallic silicides are an important component in electronic devices. They are used as ohmic contacts,[1] gate electrodes, [2] local interconnects, [3] Schottky barrier contacts, [4-7] and diffusion barriers. [8] Electronic devices are becoming smaller every year. An understanding of how silicide material behaves on these scales in needed to continue the development of smaller, more powerful silicon-based devices.

Silicides are compounds between a metal and silicon in a well-defined stoichiometry (see Figure 3.1). In this project, silicides are made by evaporating metal onto heated silicon under ultra high vacuum (UHV) conditions. In Figure 3.1, the metal atoms arrive at the silicon surface one at a time. The silicon surface is heated between 600 – 800°C which allows surface diffusion. Silicon atoms that are thermally excited from step edges onto terraces combine with the metal atoms to form the silicide compound. The silicide compound formed island structures on the heated surface of the silicon substrate, as seen in Figure 3.1. These “self assembled” structures form distinct shapes. Because the metal and silicon atoms combine slowly and in a simple relationship, the structures formed are single crystal. The shape depends on the metal used and the orientation of the silicon substrate. All the NW structures studied in this project are lying down on the

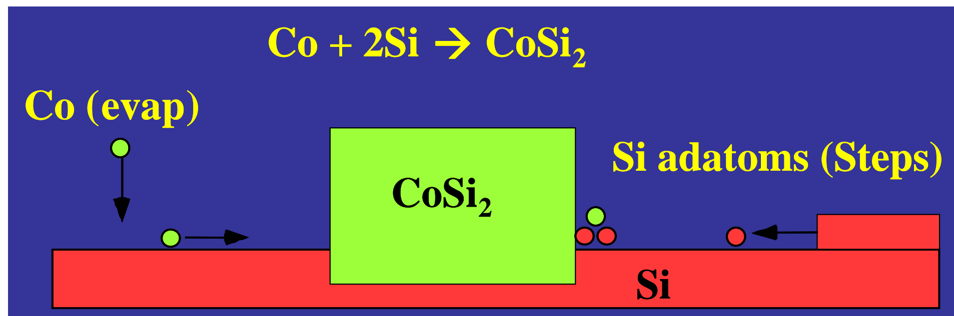

FIG. 3. 1. Schematic showing the making of $CoSi_2$ by reactive deposition. Co atoms arrive on a heated Si surface. They combine with Si adatoms that are thermally excited from the step edges.

surface. They are also embedded in the silicon surface. This makes their application with silicon devices convenient as they are already linked with the silicon substrate surface.

Figure 3.2a shows 1 monolayer (ML) cobalt (Co) deposited on Si (111) at 800°C. It shows two different silicide shapes; a triangle and a NW. The triangle silicide, labeled A, is formed on top of the silicon surface, as seen in the cross-section TEM shown in Figure 3.2c. This is an epitaxial silicide. The NW, labeled B in Figure 3.2a, has a cross-section different from the triangle, shown in Figure 3.2b. The NW is an endotaxial silicide, meaning it is embedded in the substrate. Our group has discovered and named this “endotaxial” type of structure. [19]

3.2 Rare Earth Nanowires

As mentioned earlier, the type of silicide made on a silicon surface depends on the metal that was used. The first silicide NWs observed and recorded were for rare earth metals on silicon (100), as seen in Figure 3.3a, by Preinesberger in 1998. [20, 21] The silicide NWs were made from dysprosium

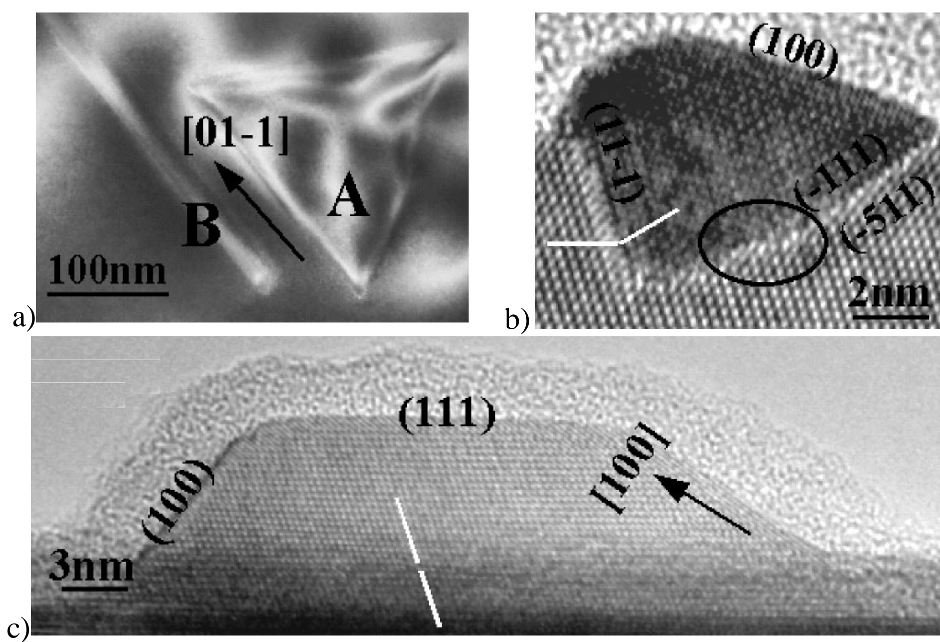

FIG. 3. 2. (a) SEM image showing an epitaxial triangular silicide (labeled A) and an endotaxial silicide NW (labeled B) on Si (111). Cross section TEM images of (b) NW and (c) triangular structure. (after He *et al*) [19]

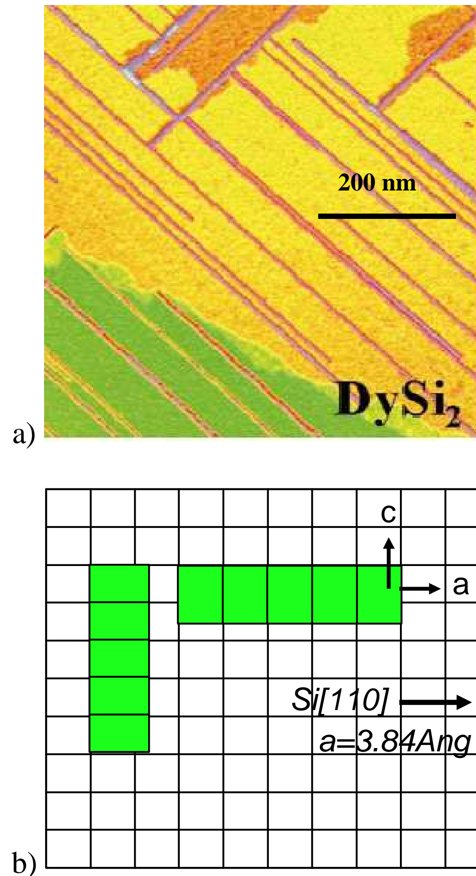

FIG. 3. 3. (a) DySi2 NWs on Si (100) [20]. (after Preinesberger *et al*) (b) Model of how asymmetric strain can cause the NW shape. Silicide structure dimension a matches Si spacing while dimension c is about 10% different. The strain along c limits growth while along a it does not, so the NW is elongated in this direction.

atoms. The rare earth silicide NWs were later found to form a crystal structure with one dimension close to the lattice spacing in the silicon substrate and the other dimension being about 10% different. During the growth of the silicide, an anisotropic strain on the surface created long, thin structures we call NWs. This can be seen in Figure 3.3b. The figure shows the mismatch along the width of the NW while the length closely matches the surrounding grid. The rare earth silicide NWs are epitaxial structures. Due to the nature of silicon (100) surfaces, the NWs grow in two orthogonal domains, based on the terrace on which they started their growth. The image in Figure 3.3a also shows that the NWs do not cross other NWs when they intersect at a perpendicular angle. They also do not cross the silicon steps. This type of NW is interesting in its formation, but was not used in this project.

3.3 Endotaxial NWs

Other metals also form silicide NW structures. [22, 23] These silicides form islands whose structure depends on temperature. In this case, the NW growth is kinetically limited and leads to the long, thin NW shape. A kinetic growth model is given as follows.

Figure 3.4a shows a NW growing with the length and the width having different growth rates. It has been shown that the ends of the NWs grow incoherently and can be described by the following equation:

$$L(t) \sim v_L \exp\left(\frac{Q_L}{kT}\right), \qquad \text{(Eq. 3.1)}$$

where v_L is the velocity of the growth at the end, Q_L is the kinetic barrier for atoms attaching to the end of the NW, and T is the temperature of the substrate.

The sides of the NW grow coherently according to the following equation:

$$W(t) \sim v_W \exp\left(\frac{Q_W}{kT}\right), \qquad \text{(Eq. 3.2)}$$

where v_W is the velocity of the growth of the side of the NW, and Q_W is the kinetic barrier for atoms attaching to the side of the NW.

Since the two equations have different rates, the length grows faster than the width. This corresponds to long thin structures that can be called NWs. The aspect ratio, L/W, depends strongly on the growth temperature. This means we can 'tune' the size of the NWs by changing the temperature. Figures 3.4b and 3.4c show cobalt silicide NWs grown by depositing 1 ML Co on Si (110) at two different temperatures, 780°C and 700°C respectively. We observe that the higher the silicon substrate temperature, the larger the NW structures are, due to lower aerial density. That is, for a given total metal thickness, the size of each island is larger if the number density is smaller.

This kinetically grown silicide NW has been named "endotaxial." [19] The inset in Figure 3.4b shows the cross-section of the NWs. The NWs are indeed single crystal structures and have embedded themselves into the top layers of the surface.

As mentioned with the rare earth NWs, the endotaxial NWs do not cross the silicon steps. Instead, when the ends of the NW reach a step, the step flows out or in to accommodate the continual growth, as seen in Figure 3.5. The end of

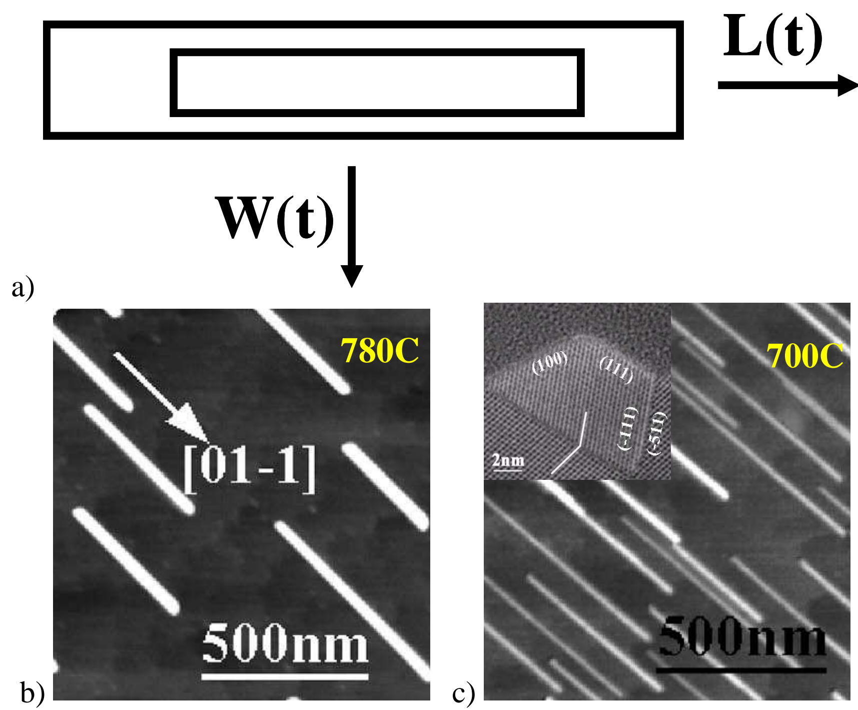

FIG. 3. 4. (a) NW with different growth rates for length and width. CoSi2 NWs on Si (110) grown at (b) 780°C and (c) 700°C with cross-section TEM (c inset). (after He *et al*) [19]

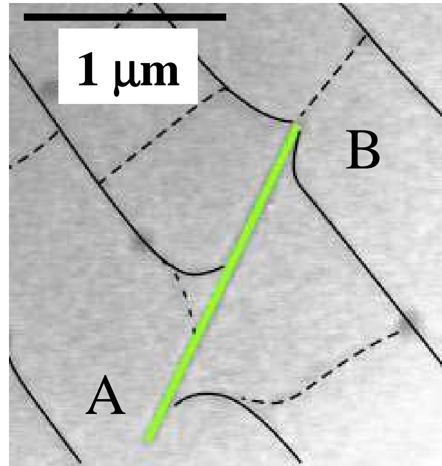

FIG. 3. 5. The Si steps (solid lines) flow in or out to accommodate the growth of NWs. NW end B is forcing a step to retreat. NW end A is forcing the step to advance. Dotted lines are impurities on the surface.

the NW located at point B in the figure has reached a silicon step and the step retreats away from the growing end. The other side, located at point A, has passed the natural location of another silicon step and has forced it to elongate to allow the NW further growth. This flexibility of step edges is made possible by the high temperature of the surface.

Endotaxial NW growth has been identified for several different metals on various orientations of silicon. Table 3.1 shows the collection of all metals reported to make NWs so far. In this dissertation we have further refined the endotaxial growth behavior for several different metals. This will be discussed later in this dissertation.

	(100)	(111)	(110)
Ti		$TiSi_2$[24, 25]	$TiSi_2$[26]
Mn		MnSi[27]	
Fe	A-$FeSi_2$[28]		FeSi[29, 30]
Co		$CoSi_2$[31]	$CoSi_2$[32]
Ni	$NiSi_2$[33]	$NiSi_2$ [34]	
Dy		$DySi_2$[35]	DySi[36]
Pt	PtSi[37]		PtSi[38, 39]
Gd	GdSi[40]	$GdSi_2$[41]	

TABLE 3. 1 List of all currently known endotaxial silicide NW systems.

4

MEASURING RESISTIVITY

4.1 Contact Resistance

Measuring the resistivity of nanostructures is challenging. Before going into details about how this was done for the endotaxial NWs, an explanation of the basic measuring techniques is required.

When measuring the resistivity of a material, electrodes need to be attached to form a circuit. At the junction point where the electrodes meet the material, a contact resistance, R_c, is formed. The current flowing through R_c causes an undesired voltage drop, which can affect the determination of material resistance. The three resistances, two R_c and the resistance of the material, are in series with each other and must be separated to obtain a good measurement. There are a few measurement techniques to measure the resistance of the material without R_c.

4.2 4-Point Method

Figure 4.1 shows a way to measure the resistivity of a material without R_c effects. This is known as the 4-point probe method. Four electrodes, or probes, are placed in contact with the material to be measured, in this case the NW. Each probe has a R_c associated with its connection. The outer two probes, P_1 and P_4, provide a known current flow, I_{14}. This same current will pass through R_c of P_1 and P_4. Probes P_2 and P_3 are placed near or in-line between P_1 and P_4. The voltage drop, V_{23}, is measured between P_2 and P_3. Since the voltage drop is measured with negligible current through P_2 and P_3, there is no voltage drop across R_c of P_2

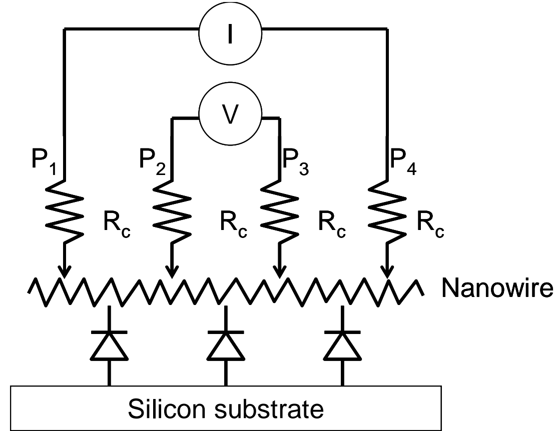

FIG. 4. 1. 4-point measuring technique for NW resistivity. Each contact has a contact resistance. A known current is passed through the outer two contacts and voltage is measured on the inner two. The NW is separated from the Si substrate by a Schottky barrier which behaves as a diode.

and P_3. This will eliminate the contributions and corresponding uncertainties associated with R_c between the NW and the probes. In this way a 4-point resistance can be measured as,

$$R_{4pt} = \frac{V_{23}}{I_{14}}. \qquad \text{(Eq. 4.1)}$$

Assuming uniform current density across a constant cross-sectional area A, the resistivity, ρ, can be calculated as

$$\rho = R_{4pt}\left(\frac{A}{L_{23}}\right), \qquad \text{(Eq. 4.2)}$$

where L_{23} is the spacing between the voltage probes, P_2 and P_3.

A note should be made in regards to this 4-point probe measuring technique. This technique is often used to measure the sheet resistances of a thin film, which is given as

$$R_{square} \propto \frac{\rho}{t} \quad \text{(Eq. 4.3)}$$

where t is the thickness of the film. Various probe configurations may be used. The two most common geometries are linear (in-line), as in our application, or square. Both configurations have been demonstrated with a multi-tip UHV STM instrument. [42]

In our case, we have a metallic NW resting on a semiconducting substrate. In this instance, special care must be taken to make sure the current is only flowing through the NW and not the surrounding substrate as well. Fortunately, in this case, the NWs are electrically isolated from the substrate by a Schottky barrier. For example, in the case of $CoSi_2$ NWs on Si (110), we found $R_{SB} \sim 10^7\ \Omega$ even though the substrate was highly doped, with $\rho_{Si} \sim 1\ \mu\Omega$ cm. The tungsten tip of the STM probe is also isolated from the substrate by a different Schottky barrier. This means that overlapping contact between the tip and substrate will not cause extra current flow. The Schottky barrier isolation is represented in equivalent circuit diagrams as small diodes between the NW and substrate.

4.3 2-Point Variable-Distance Method

A second method used to measure resistivity without the uncertainty of R_c is a 2-point variable-distance method. Both the current and the voltage drop are measured with the same two probes. By adjusting the distance L between the probes, R_c can be removed, since we have

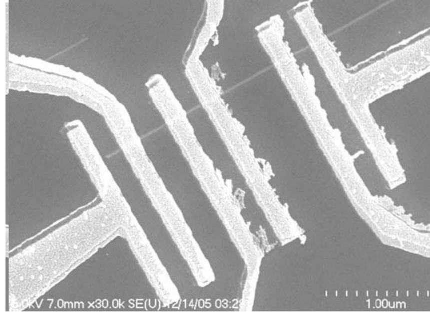

FIG. 4. 2. SEM image of contacts on a NW. The contacts were added ex situ (after growth of the NWs in UHV) by electron beam lithography.

$$R_{2pt}(L) = \frac{V}{I} = R_{NW} + 2R_c = \frac{\rho}{A}L + 2R_c\,, \qquad \text{(Eq. 4.4)}$$

where R_{NW} is taken from Eq. 2.6.

A plot of $R_{2pt}(L)$ will show a linear increase for R vs L as given in Eq. 4.4. The slope is used to find ρ while the y-intercept gives R_c.

A concern arises if R_c is similar in size to R_{NW}, since uncertainties in R_c can then dominate. If R_c is small compared to R_{NW}, this method works well to calculate ρ.

4.4 Ex Situ Resistivity Measurements

One way in which the 4-point probe method has been used is shown in Figure 4.2. In this image the silicide NWs were made in UHV. They were transferred through air to the CSSER nanofab where contacts were added using electron beam lithography (EBL). One difficulty with these ex situ procedures is the inevitable formation of insulating oxides between the NWs and the electrical contacts. This may cause a large R_c that can dominate the resistivity measurements, even in 4-point mode. Figure 4.2 is a SEM image showing five

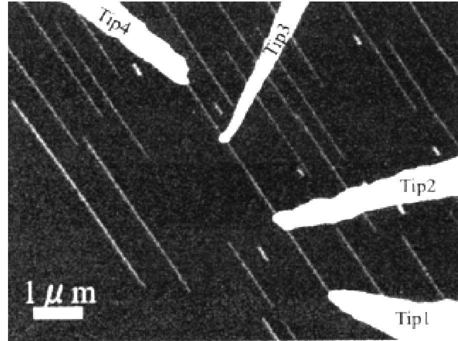

FIG. 4. 3. SEM image of Professor Hasegawa's multi-probe STM being used as a 4-point probe to measure the resistivity of a $CoSi_2$ NW on Si (110). The inner two contacts can also be used in a 2-point variable-spacing configuration. Comparison between the 4-point and "hot" 2-point resistance between probes 2 and 3 yielded $R_{4pt}=207\Omega$ and $R_{2pt}=237\Omega$ resulting in $Rc=30\Omega$. [43] (after Okino *et al*)

contacts to a single NW. The image shows the contrast in the roughness of the contacts compared to the straightness of the NW. This image illustrates that self-assembled nanostructures can be better than fabricated structures.

Another concern with these contacts is the large area of direct contact between the probes and the silicon substrate, which can cause significant amounts of "leakage" current to flow through the silicon. This leakage current can be avoided by cooling the semiconducting substrate to freeze out the carriers.

In situ procedures are desired to eliminate the extrinsic contact issues described above. There are several different ways to perform in situ measurements.

4.5 Multi Probe STM Instrument

Professor Hasegawa has pioneered the development of a multi-probe STM that can be used to measure nanoscale materials. [43] Figure 4.3 is an SEM image

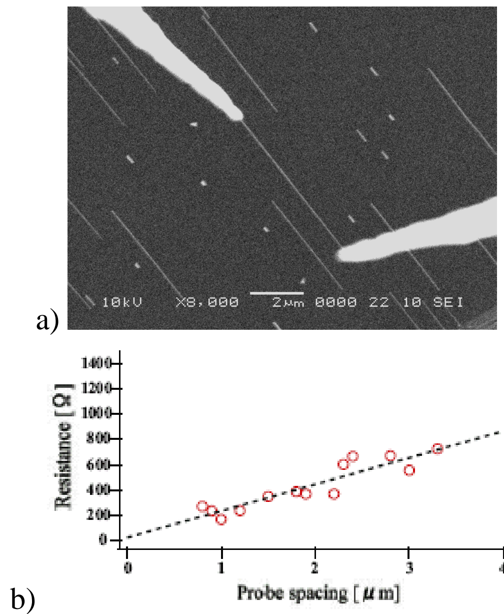

FIG. 4. 4. (a) SEM of Professor Hasegawa's multi-probe STM being used as a 2-pt variable distance probe on 30 nm wide CoSi2 NWs on Si (110). Measurements were taken at T=300K. (b) Resistance vs probe spacing data. [43] (after Okino *et al*)

that shows four separate STM tips contacting a single cobalt silicide NW. The authors were able to make and measure the NWs without transfer through air. Since the tips to the STM are designed to be contact probes they are not used for imaging. Instead, the SEM is used to image the sample and for positioning the probes. This machine can also be used for the 2-point variable-distance method, as shown in Figure 4.4a. In this instance, only 2 tips are contacting the NW. A resistance vs probe spacing plot is shown in Figure 4.4b.

The Hasegawa group has developed STM tips with carbon nanotubes (CNT) at their ends. [44] Such tips are available for purchase. Figure 4.5 is an SEM image of four CNT tips contacting a single silicide NW. The large aspect ratio of the CNT tips allows for a very close spacing between the probes. This

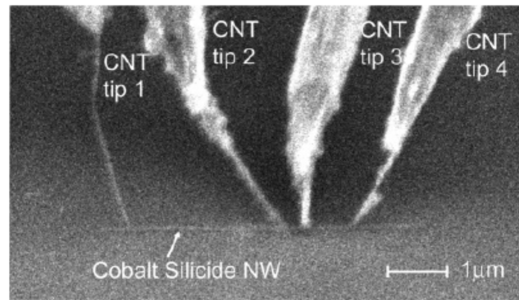

FIG. 4. 5. SEM image of Professor Hasegawa's multi-probe STM being used as a 4-point probe to measure the resistivity of a $CoSi_2$ NW. The tips have PtIr coated carbon naotubes (CNT) ends. [44] (after Yoshimoto *et al*)

closer spacing allowed the measurement of electron scattering from a single grain boundary in damascene copper lines. [45]

A major goal in this dissertation is to develop an in situ method to measure ρ of NWs. This is done with a single probe STM and a fixed contact pad on the substrate. The tip is moved along the NW to provide the variable spacing needed for R(L) measurements. Images of the sample are done with the STM tip and can provide atomic resolution of the NW and its surroundings. The sample can be cooled or heated as desired for measurements. This is discussed in more detail in the next chapter.

5

INSTRUMENTATION AND SAMPLE PREPARATION METHODS

5.1 STM

The instrument used for imaging and measurements was a UHV 300 from RHK Technologies. Figure 5.1 shows a schematic of the UHV 300 from the company webpage. [46] Within the UHV chamber is a storage elevator that can accommodate up to three tips and three samples. A load lock on the side of the chamber allows transfer of tips and samples without opening the chamber itself.

The STM measurement stage is equipped with a heater coil below the sample. A copper braid connecting the stage to a liquid nitrogen tank allows for sample cooling. In our experiments, we have used temperatures in the range T = 130 - 400 K. A thermocouple is located near the sample holder to measure T.

This STM uses a 'Beetle' type scanning head, as shown in Figure 5.2a. This is named for the nature of the coarse approach. The scanning tip resides above the sample and hangs down along with three walking legs. The sample stage has three inclined planes for the legs to walk up or down. The vertical motion (perpendicular to the sample surface) is done with a tangential stick-slip motion of the piezo legs. Movement in the XY plane (parallel to the sample surface) is done with combined radial/tangential motions of the piezo legs.

Figure 5.2b shows a top view of the sample holder. Notice the three separate inclined planes for the tip holder to walk up, down or sideways. The sample itself is held by a pair of sapphire rings. The inner diameter of the sapphire rings is 5mm. The outer diameter is 10 mm. Samples need to be less than 1 cm to

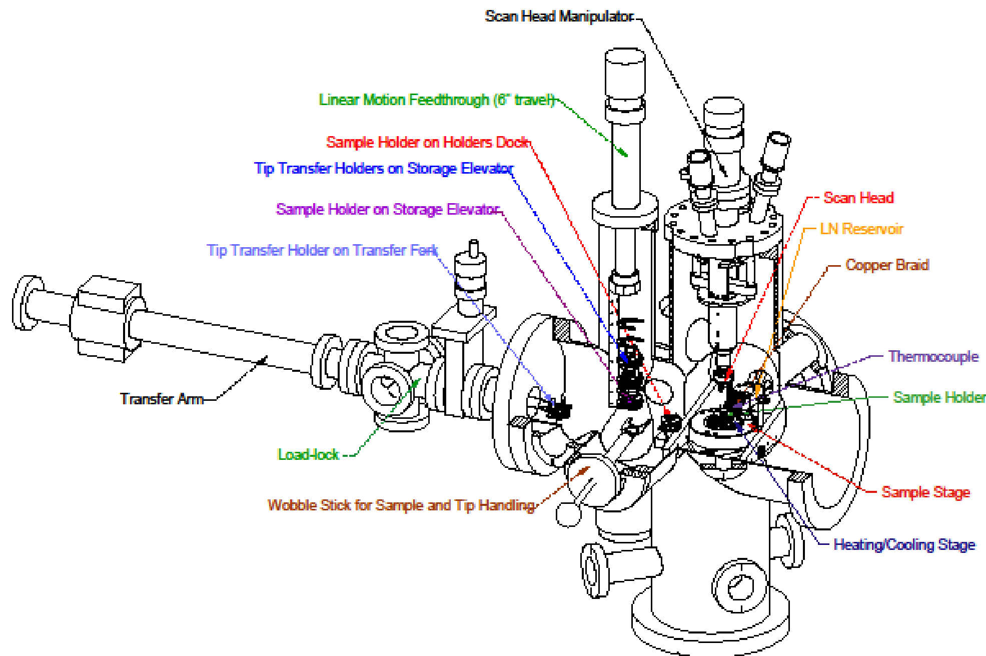

FIG. 5. 1. RHK UHV 300 [46]

accommodate these sizes. All processing on the sample, including making NWs and measuring ρ, must be done within the 5 mm inner diameter.

Sticking out the left side of the sample holder are electrical contacts that are electrically isolated from the main body of the sample holder. These contacts connect to the sample through a tantalum clip. Another tantalum clip connects the sample to the main body of the sample holder. In this way the current can be passed through the sample for resistive heating during NW growth or for cleaning of the substrate.

The STM is controlled via a RHK SPM 100 controller operated via a computer with Windows-based “SPM 32” software from RHK. The files generated by the software are processed through the use of the open source and

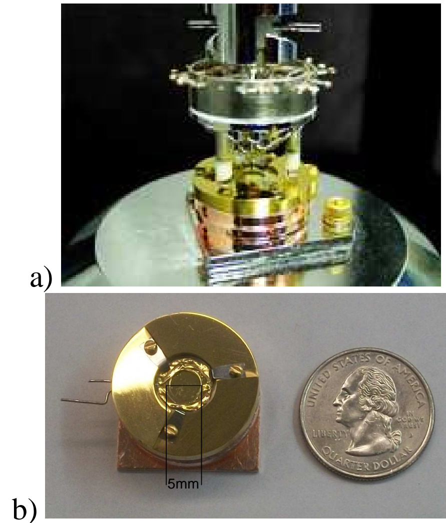

FIG. 5. 2. (a) Image of ‘Beetle’ type STM. Tip hangs above sample. Legs walk down incline to bring tip to sample. (b) Top view of STM sample holder showing electrical contacts sticking out on left. The sapphire ring has inner diameter of 5mm.

free software, Gwyddion. [47] Gwyddion provides an easy way to analyze images from most commercial scanners. At times, a Varian AFM was used for larger scan areas done ex situ. Gwyddion provided the ability to analyze all the files from the different scanners using the same program.

5.2 Tip Preparation

The tips used for imaging are made by electrochemically etching a 0.01 in diameter polycrystalline tungsten wire. [48-50] The etching solution is a 5 molar KOH solution made by adding 10 pellets, each pellet about 0.111g, to 15 mL distilled water. Two methods of etching tips were used in the course of this project. Figure 5.3 shows a schematic for the first method. A control power supply was used to pass a current through the tip, the solution and a counter electrode. Etching occurs where the tip enters the solution at the surface. The

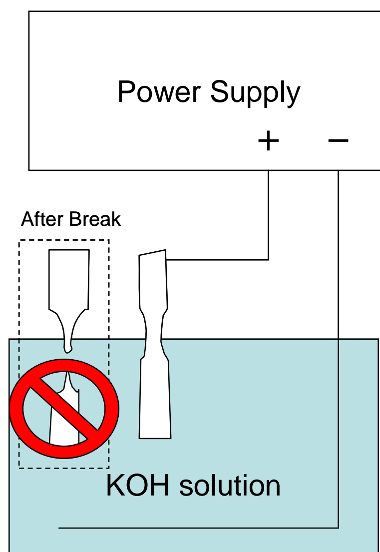

FIG. 5. 3. Schematic of tip etching by first method. This current flows from W wire through KOH solution to submerged electrode. Etching occurs on surface of solution to form a decaying neck. After the neck breaks the top is used for STM tip and the bottom is discarded.

etching creates a bottle neck in the tungsten wire as time progresses. As the neck thins over time, the weight of the tungsten wire fully submerged in the solution causes the wire to stretch and break. The lower portion will fall to the bottom of the solution container and is discarded. This appears pictorially on the left side of the image.

If etching is allowed to continue, the tip will dull from over etching. Therefore, the current needs to be shut off extremely fast after the wire breaks. This fast shut-off must be done with an electronic shut-off, which is triggered by the large decrease in current when the tip separates. Figure 5.4 shows the current versus time for the etching process. At approximately 800 seconds the sudden

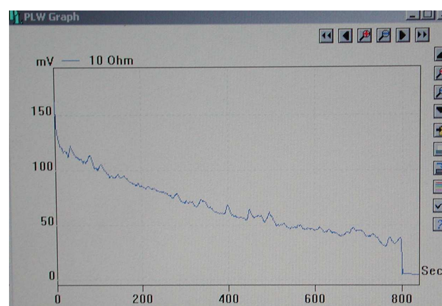

FIG. 5. 4. Current vs time during etching of tip. At around 800 seconds the neck breaks and the etching is quickly turned off.

drop in the current gives evidence of the break. An electronic shut off quickly turned off the current to prevent over etching of the sharp tip.

Figure 5.5 shows an optical image of a typical etched tip from this method. The timing of the etching needs to be slow enough to allow smooth etching of the metal. Even so, multiple curves associated with the etching are often seen along the neck of the tip. The inset shows a closer view of the end of the tip. The radius of the tip is typically below 50 nm.

Even with the electronic shut-off, the tips were often dulled by over-etching. This was caused by a non-suitable threshold for the electronic shut off. Therefore, another way to etch STM tips was implemented.

Figure 5.6 shows a schematic for the preferred etching method. This method uses the fallen tungsten piece as the STM tip. To etch the tips the KOH solution is suspended as a film within a nickel wire loop with a diameter of 11 mm. The tungsten wire is pressed through the film, sticking out 1.2 – 1.5 cm below the film. As with the original etching process, etching mainly occurs at the

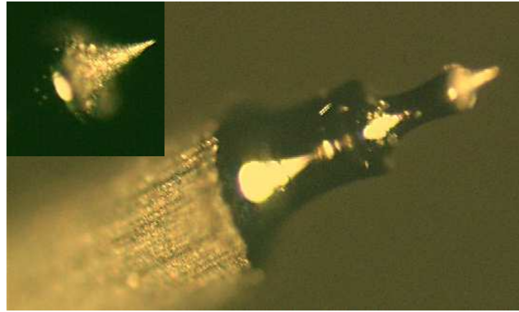

FIG. 5. 5. Optical image of W wire etched with first etching method. Inset is a closer view of the tip.

top of the submerged tungsten although the entire submerged tungsten is also etched. Over time the weight of the lower tungsten will cause a final stretching and breaking of the neck, resulting in the lower piece falling away from the film. This appears in the left side of Figure 5.6. Since the fallen part is used, there is no need for a fast shut off. The upper portion can be used to make another tip (with a new break point).

The new tip is protected from colliding with the table using a container filled with shaving cream that gently catches the tungsten wire. The shaving cream is removed by rinsing the tip with distilled water. An optical microscope is used for a first check of tip sharpness. The tip is considered good when interference fringes extend smoothly beyond the “visible” tip end. These sharp tips have been verified with SEM imaging as seen in Figure 5.7 with an end radius less than 40 nm.

Figure 5.8 shows an image of the present tip-etching setup. The tungsten wire and the nickel loop are held in place by magnet clamps. This allows for relative ease of adjusting their locations to align with each other.

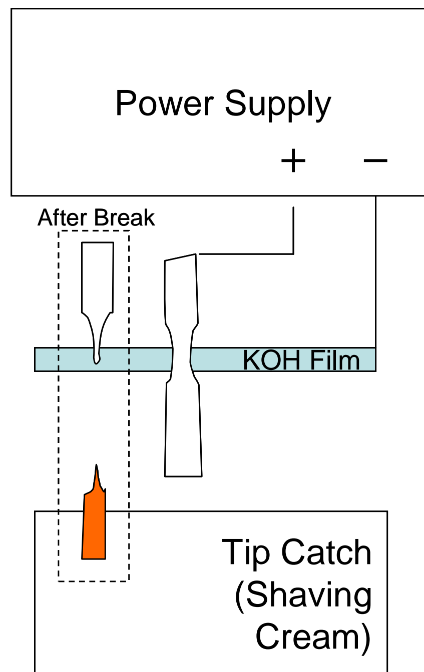

FIG. 5. 6. Schematic of tip etching by second method. The current passes from W wire though the KOH film to the other electrode. The etched neck forms in film. After the neck breaks the lower portion falls into shaving cream and is used as STM tip. The upper portion is not used as STM tip.

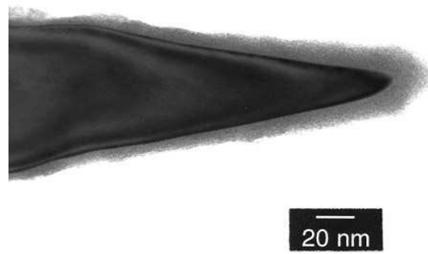

FIG. 5. 7. SEM image of tip etched with second method.

Before a tip can be placed in the STM chamber and be used, it is annealed and checked for sharpness. Even with the new system for etching tips there is no guarantee of a good STM tip. The system in place produces good tips approximately 80% of the time.

The tip is annealed by heating in a turbo-pumped chamber with pressure about 10^{-6} Torr. Figure 5.9a shows how the tip is attached to a tantalum bar and oriented toward a metal plate anode. Current through the tantalum bar causes it to heat up. By conduction, the tip is also heated. The ideal temperature for annealing the tip to remove oxide layers is 800°C. Once this is accomplished the tip is allowed to cool and is checked for sharpness.

It is useful to characterize the STM tip by measuring its field emitting behavior. For a counter electrode far away, the electric field at the surface of the tip is given by $F \sim V/R$, where R is the local tip radius and V is the negative bias voltage applied to the tip. The total current can be estimated from the Fowler Nordheim expression [51]

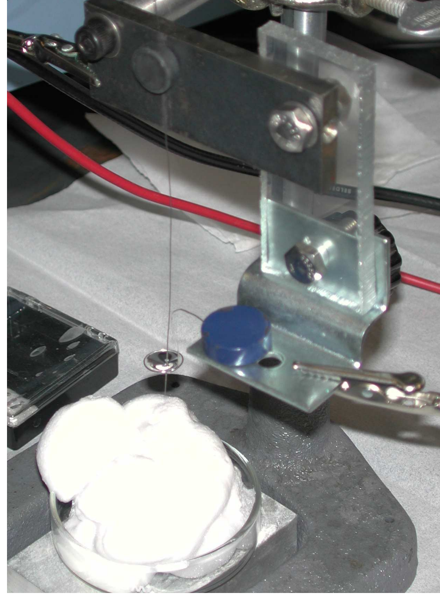

FIG. 5. 8. Current setup for STM etching. The W wire and Ni loop holding KOH film are held by magnets for ease of alignment. The shaving cream below will catch fallen tip after etched neck breaks.

$$J_{FN} = \frac{C_1}{\alpha^2}\left(\mu/\Phi\right)^{3/2} F^2 \exp\left(-C_2 \Phi^{3/2} \alpha / F\right), \qquad \text{(Eq 5.1)}$$

where J(Amp/area) is the current density, α is a correction factor for image potential effects, μ(eV) is the chemical potential, Φ(eV) is the work function, F(V/nm) is the field at the surface, $C_1 = 6.2x10^6 A/V^2$ and $C_2 = 6.8$ V/nm-eV$^{3/2}$. In practice, we measure a "field emission threshold," V_{FET}, which we define as the bias voltage required for $I_{FE} = 20nA$. A plot of V_{FET} vs. R is shown in Figure 5.10. A good tip has $V_{FET} < 400V$. Such tips can produce "atomic resolution" images. Tips with $400V < V_{FET} < 1000V$ are also usable for ρ measurements although they cannot give “atomic resolution” images. Tips with $V_{FET} > 1000V$ are discarded. It is important to note that the tip radius inferred from V_{FET} corresponds

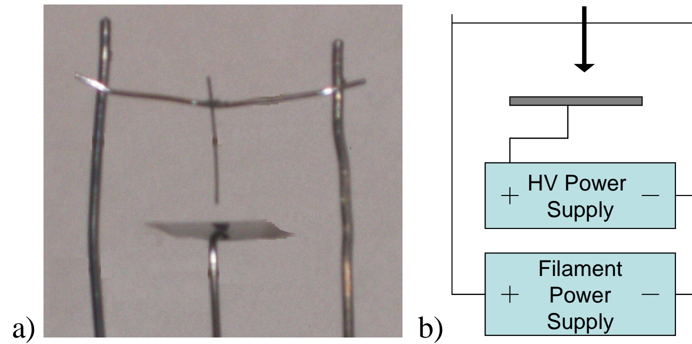

FIG. 5. 9. (a) Tip attached to Ta heater bar for annealing. Tip faces down toward anode for field emission check of tip sharpness. (b) The schematic of annealing process and field emission process. All done in turbo system at 10^{-6} Torr.

to a macroscopic radius R, as seen from far away, while the local radius that affects imaging can be much smaller.

After the sharpness of the tip has been verified, it is mounted into a tip holder and placed within the STM chamber. This is done quickly after annealing as the tip must be transferred through air. The oxide that forms as a result of the tip transfer is removed by field emission conditioning within the STM chamber. As long as the transfer takes less than 30 minutes, the new oxide is easily removed within the chamber.

5.3 Contact Pad

The STM tip is the movable contact to the NWs. The second contact is a fixed metal pad that is added to the sample after growth of the NWs. This contact pad must have a sharp edge to allow well defined R(L) measurements. The contact pad is added by shadow evaporation. Figure 5.11 shows a schematic for how this is done. The shadow mask is made from cleaved gallium arsenide (100). Gallium arsenide is used because of its excellent cleaving behavior, which leaves

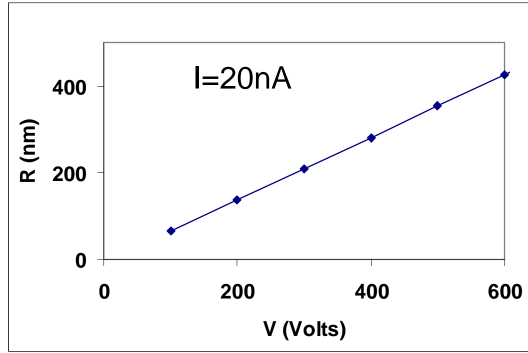

FIG. 5. 10. V_{FET} vs tip radius R for I=20nA.

an extremely sharp edge. The sample is brought close to the shadow mask slowly, and placed in direct contact with the mask. The inherent rough quality of the sample and the shadow mask typically results in a gap which is estimated approximately at 1 μm. This is seen in Figure 5.12 which displays a SEM image of the sample-mask interface. The inset is a close up displaying the 1 μm gap between the sample and the mask.

The metal filament used to deposit the contact pad is carefully oriented parallel to the shadow mask edge. This provides a small effective source size in the direction perpendicular to the edge, while providing a large total flux for the contact pad. The linear filament will also last longer than a point source.

The geometry results in

$$\frac{w_1}{D_1} = \frac{w_2}{D_2}, \qquad \text{(Eq. 5.2)}$$

where w_1 is the width of the filament, D_1 is the distance of the filament from the sample-mask interface, D_2 is the gap size between the sample and mask and w_2 is the resulting width of the film edge. The value of w_1 will be slightly larger than

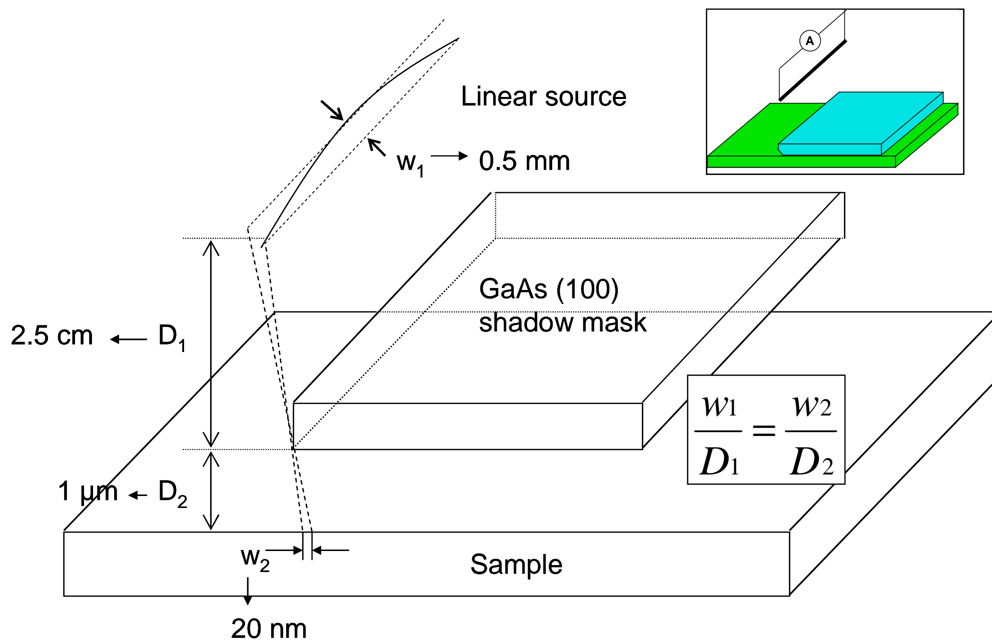

FIG. 5. 11. Schematic displaying dimensions during contact pad deposition. Filament is a 0.5 mm thick linear source orientated parallel to the mask – sample interface 2.5 cm away. The mask sits 1 μm above the sample. Geometrically, the pad edge can be 20 nm. The inset displays color image without values.

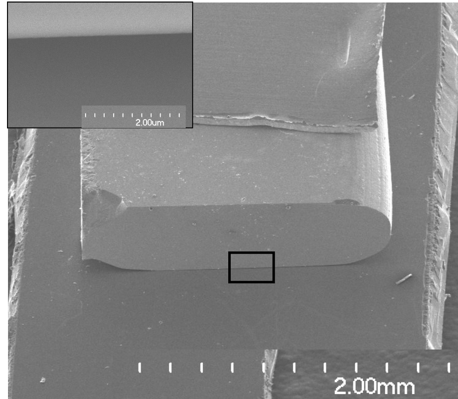

FIG. 5. 12. SEM image verifying mask – sample interface. Inset is enlarged interface showing gap size of 1 μm between mask and sample.

the diameter of the wire used, since it also includes alignment errors. With w_1 = 0.8 mm, D_1 = 2.5 cm, and D_2 ~ 1 μm, we calculate w_2 ~ 30 nm. This is the theoretical limit for the given parameters. In practice, contact pads with edges as small as 50 nm are possible.

This project explored gold, platinum, cobalt, and titanium for the contact pad. Figure 5.13 displays the resulting edges. The first metal that was used for the contact pad was gold. (Figure 5.13a) Gold is simple to evaporate and it provides an inert film. The consistencies of the thickness amounting to over 20 nm were needed in order to have reasonable conductivity. The gold formed large grains resulting in a rough film. The large grain sizes of the film also caused the film to have a large sheet resistance.

Platinum was found to produce smaller grain sizes (Figure 5.13b) and had a lower resistance than gold, for thin films. A difficulty arose, however, in the stability of the film, which was possibly due to diffusion and intermixing of

platinum with the substrate. Within a day in residual vacuum, the sheet resistance of the film increased by two orders of magnitude. This made the sheet resistance larger than the NW resistances, making it impossible to accurately measure the resistance of the NWs.

Cobalt (Figure 5.13c) behaved similar to the platinum film. It also had small grain size and low sheet resistance for thin films. However, cobalt also became unstable, like the platinum films.

Lastly, titanium was tested. (Figure 5.13d) Titanium has a small grain size and low sheet resistance. In addition, this film also provided the stability that the other metals lacked. The low resistance of the film lasted over two months, at which point the sample was removed from the STM chamber. A summary of each of the films is shown in Table 5.1.

5.4 Sample Preparation Chamber

A significant component of this project was the design and construction of a sample preparation chamber to grow the NWs and deposit the contact pad in UHV. Figure 5.14 shows the design of the sample preparation stage. It was placed in the load lock chamber which had a separate ion pump to achieve the required low pressure of 10^{-9} Torr.

The STM has multiple sample holders that fit onto the imaging stage. They are hollow. The preparation stage was designed with a support post that fits snuggly into this hollow. A heater is located within the post to degas the entire assembly after exposure to air as well as provide a way to heat the sample. To the

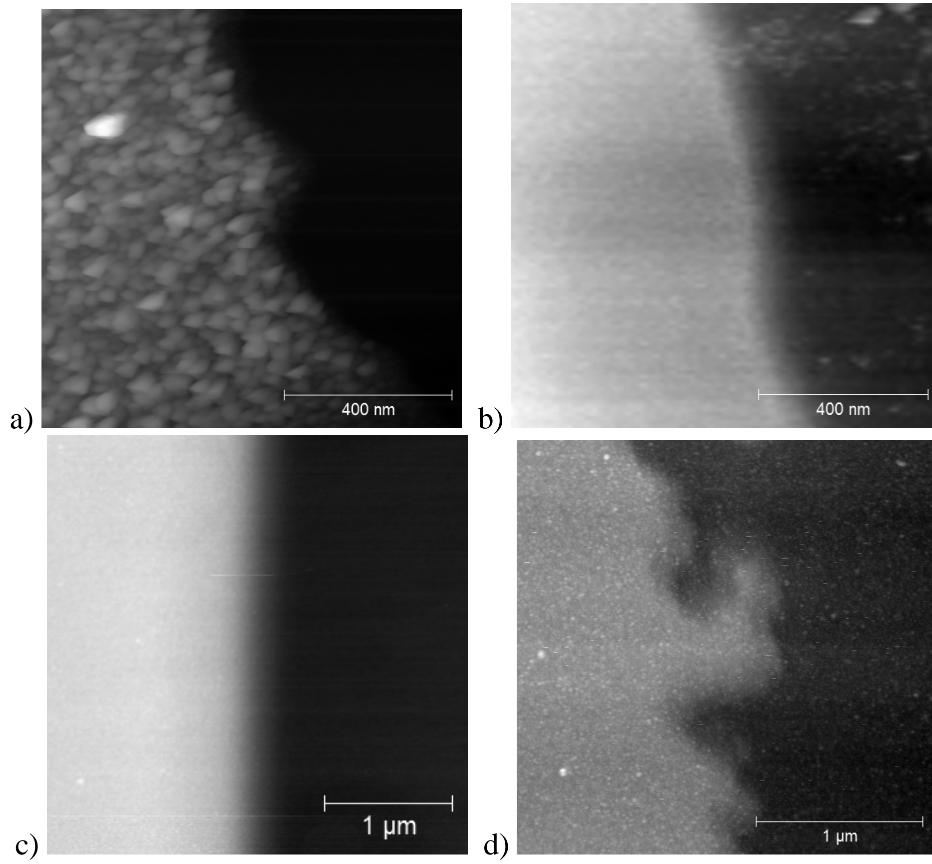

FIG. 5. 13. Contact pad edges made from (a) Au, (b) Pt, (c) Co, and (d) Ti.

	Thickness (nm)	Vertical Feature Size (nm)	Lateral Feature Size (nm)	R□ (Ω/□)	Best Edge (nm)	Stability
Au	25±15	40±20	45±25	700	80	
Pt	18±12	10±5	20±15	400	87	Poor
Co	13±8	1±0.5	30±10	500	90	Poor
Ti	8±5	1±0.5	15±10	200	48	Good

TABLE 5. 1. Results of contact pad edges from Au, Pt, Co, and Ti. The stability column tells if film stays low resistive for long periods of time (> 1 day).

left of the center column is a copper fork that is used to make electrical contact to the sample holder. This helps orient the sample relative to the other items on the assembly as well as providing for current through the sample. The center column can be moved vertically to allow the sample to be brought closer to the shadow mask, which is located above it.

The top of the assembly is open to accommodate a far away filament that is used for NW growth. The filament is not shown since it is over 15 cm above the sample. Also located far away from the sample, and close to the NW-making filament, is the crystal growth monitor, which is used to verify the thickness that is deposited.

At the top right of the image is the linear filament used in making the contact pad. It is placed slightly to the side to prevent it from shadowing the sample from the filament used in NW growth and to allow an easier line of sight to the sample-mask interface. With this, the bottom edge of the mask determines the pad edge and not the top edge of the mask.

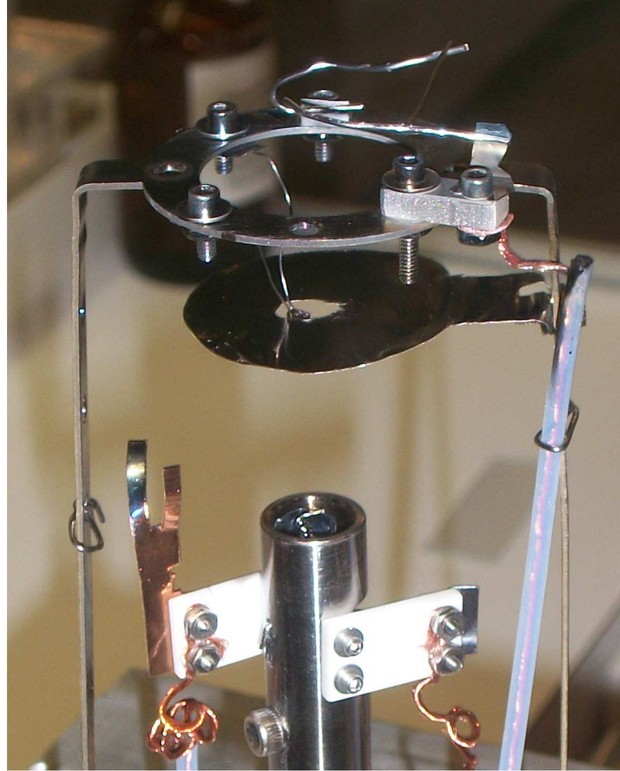

FIG. 5. 14. Sample prep chamber. The STM sample holder sits on center column. Within the column is a heater filament. The copper fork on left attaches to the sample holder's electrical contacts. The column moved vertically to approach the GaAs mask hanging from above. The larger Mo mask protects sample holder. The Ti linear filament is located at the top right of image.

A large mask is placed above the sample holder with a hole cut in its center. This hole protects the sample holder while still providing access to the center region of the sample. Hanging down within the hole is the gallium arsenide mask. The mask must be directed in a way that it contacts the exposed area of the sample, less than 5 mm diameter. The shadow mask must also be positioned to allow enough open space on the sample to provide a sufficient contact pad.

All of these parts are carefully aligned in air before inserting into the vacuum. This provides a simple way to ensure the orientations are correct and the wires are electrically connected to the correct leads without shorting.

5.5 Sample Fabrication

The fabrication process for the sample is displayed in Figure 5.15. The figure labels the sequence of events. First, the sample needs to be electrically connected to the STM sample holder. As mentioned above, tantalum clips are placed on the outer edges of the sample to connect it to the sample holder's body and the electrical contacts sticking out the side. It is hard to make contact between the clips and the evaporated pad, due to shadowing effects. Therefore, tantalum pads are made first on the outside edges of the sample. Approximately 50 nm of tantalum was deposited on the outsides. The tantalum reacted with the silicon during the 1200°C flashes to provide a stable silicide pad with $R < 50\ \Omega$. The tantalum silicide pad must extend inside the inner diameter of the sapphire ring. When the sample is placed in the holder, care is taken to expose the pad. The sample is now placed into the chamber.

Once in the chamber, the sample is degassed at 500°C for over 2 hours. Following the degassing the sample is flashed several times to 1200 – 1250°C for a few seconds each time to minimize pressure changes inside the chamber. These flash heatings clean the sample surface by removing carbon and oxygen. The STM scans are used to verify the sample cleanliness by checking for smooth steps.

The sample is then heated to the desired NW growth temperature (600-800°C) and the metal atoms are deposited to form the NW silicides. STM imaging

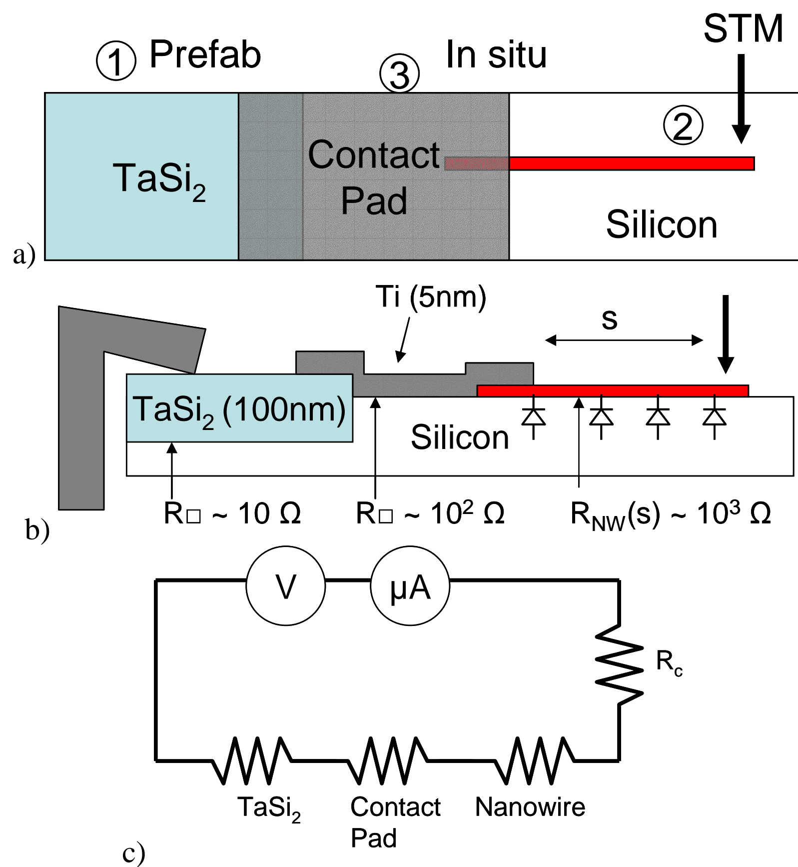

FIG. 5. 15. Schematic of fabricated sample: (a) top, (b) side. First, Ta is deposited to form 50 nm thick pads on side. The Ta clips attach sample to STM sample holder. During 1200°C flashes Ti reacts with Si to form 100 nm thick silicide with R < 30 Ω. Second, NWs are made. Third, the contact pad is deposited to connect NWs to $TaSi_2$ pad. STM tip connects with NW to complete circuit shown in (c).

is used again to verify the size and the number of NWs on the surface. After that, the sample is ready for the final component: the contact pad.

Once the sample is complete, the STM is used to scan the surface and find NWs that project out from under the contact pad. Once these NWs are found the STM tip can be placed along the exposed part of the NW and a resistance measurement can be made. The electrical circuit is shown in Figure 5.15c. The STM tip is then moved along the exposed parts of the NW to collect data for resistance vs position along the NW. In this way, the STM tip and contact pad become a 2-point variable distance probe. Resistivity ρ is then determined from the slope of R(L).

5.6 Controlled Approach to Contact

R_c at the tip is the only component that may change once the sample is completely fabricated. Care must be taken not to compromise the NW or the tip during contacts. Therefore, a consistent method for contacting the NWs with the tip needs to be established.

The STM tip is already known to have a small local radius. For small bias voltage, the gap is small (<1nm) and imaging proceeds with small asperities on the tip, as will be discussed later. Multiple contacts with the surface may cause the tip to become dull and the radius to increase. Also, asperities may cause "ghost images" to appear in the scans. Ghost images are defined as tall features on the surface that are replicated one or more times in the image with a small lateral and vertical offset to the original feature. This reflects a convolution of the real surface shape with a multi-point tip shape. In the case of only 2-3 ghost images,

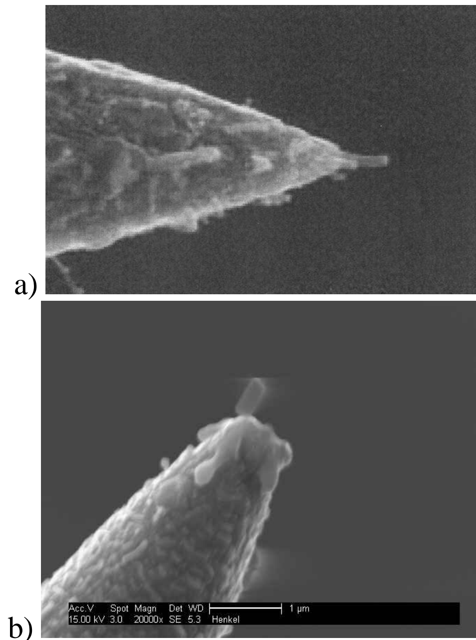

FIG. 5. 16. SEM images of carbon nanotube on end of W etched tip (a) before contacts and (b) after over 100 contacts with sample. CNT still at end of tip.

the resistance measurement can still be done, since the precise nature of the metal-metal contact (tip to NW) in not critical. However, if many ghost images appear, resistance measurements are impossible and the tip needs to be changed.

CNT tips were tested for use as electrical nanoprobes, with the intention of reducing the dulling that normally occurs with tungsten tips. Several CNT tips were received from Professor Hasegawa. An SEM image of a CNT tip is shown in Figure 5.16a. These tips were studied for their usefulness in making measurements of ρ.

CNT tips have a small radius, giving great contact accuracy. After more than 100 contacts, the tip was found to still be sharp, with the CNT mostly

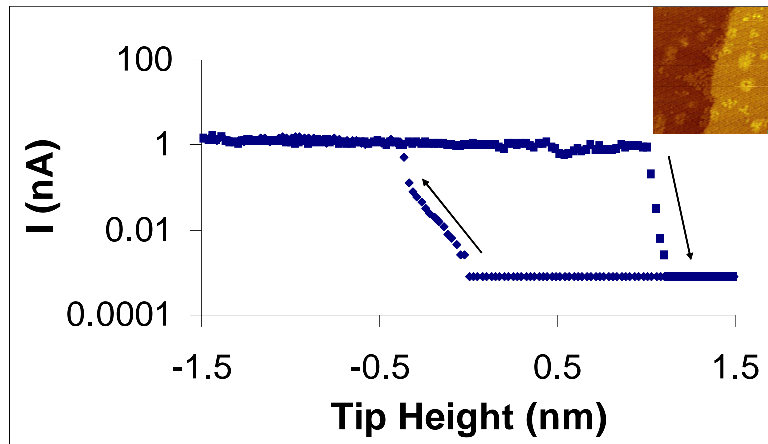

FIG. 5. 17. Current vs z with CNT tip. Inset is an image scanned by a tip after repeated contact with the surface showing atomic resolution is still possible.

undamaged, as judged by the quality of STM images. Figure 5.16b shows an SEM image of a CNT tip after many contacts and resistance measurements in the STM. Notice that the CNT is still prominent at the end of the tip, although it is considerably shorter than normal.

When either the tungsten etched tip or the CNT tip was brought into contact with the surface, it often displayed a phenomenon of "jump to contact." [52, 53] From the recorded current vs the gap size, I vs z as in Figure 5.17, we see that contact is made abruptly around 5 Angstroms beyond the tunneling point (1nA at 10mV bias). To test the durability of the CNT, the tip was pressed an additional 10 Angstroms into the surface, for a total of 15 Angstroms beyond tunneling. When the tip was removed from the sample a hysteresis was observed. This is common for a nanoscale contact. This hysteresis is due to a bridge forming between the tip and sample and stretching as the tip is pulled away from the surface. Material transfer is common when this happens. The CNT remains at the

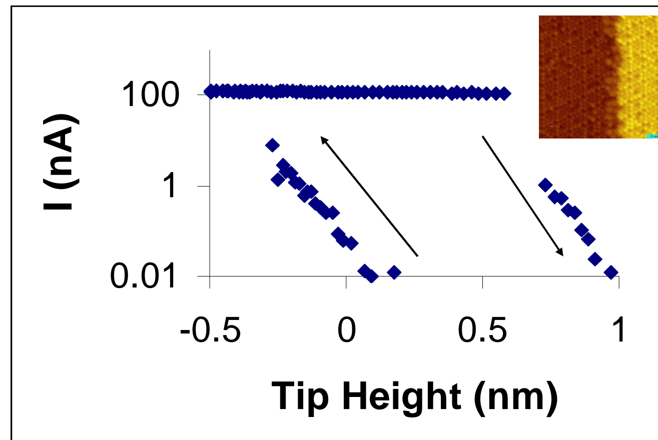

FIG. 5. 18. Current vs z with W etched tip. The inset is a scanned image after the repeated gentle contacts displaying the atomic resolution is still possible.

end of the tip, as evidenced by the high quality STM image seen in the inset of Figure 5.17, and by the SEM image of Figure 5.16b.

The CNT remains an excellent imager and scanner after many contacts. Unfortunately, we found the resistance of the CNT to be too large for our measurements. The resistance of the CNT was $R_{CNT} \sim 10^6\ \Omega$. This is a significant amount larger than the resistance of the NW we desire to measure. By contrast, the etched tungsten tips have a low contact resistance of $R_c = 50\ \Omega$.
These tips also displayed "jump to contact," as seen in Figure 5.18. Sufficient contact was made with the NWs when the tip was pressed 5 Angstroms beyond tunneling, as seen in the figure. If the tip was pressed further into the surface, damage to the tip resulted in dulling. This result required exchange of the tip. As long as the contact is gentle (limited to 5 Angstroms beyond tunneling), the tip can withstand numerous contacts. "Atomic resolution" is not necessary for these

experiments. Step resolution, as seen in the inset image in the Figure 5.18, is adequate.

To quickly collect and analyze the data, a LabView Virtual Instrument (VI) was constructed, with a Front Panel as shown in Figure 5.19 and the block diagram as displayed in Figure 5.20. This program will record I(z) during each approach to contact. Once the tip makes contact, the position and resistance are recorded, R(x,y,z). The VI also undoes the log response of the pre-amplifier. Once all measurements are collected, a file is written which can be analyzed in Excel, or other spreadsheet programs.

Page 1 STM v8p2

STM_v8p2a.vi
C:\Documents and Settings\Student\Desktop\STM_v8p2a.vi
Last modified on 6/8/2011 at 5:09 PM
Printed on 7/5/2011 at 12:24 PM

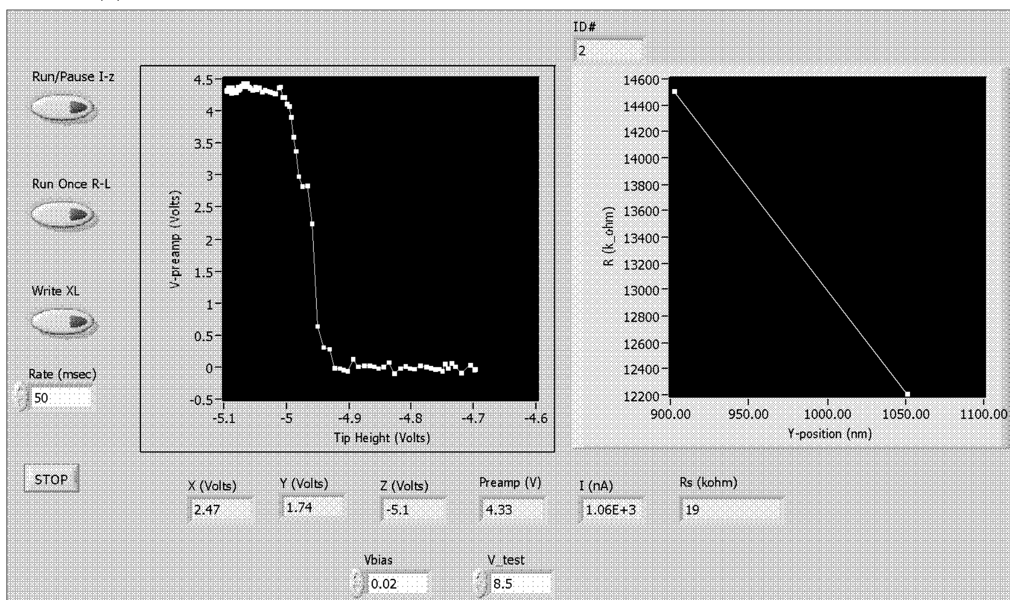

FIG. 5. 19. Front Panel of the LabView VI constructed to follow I vs z during tip approach and capture R(x,y,z) measurements.

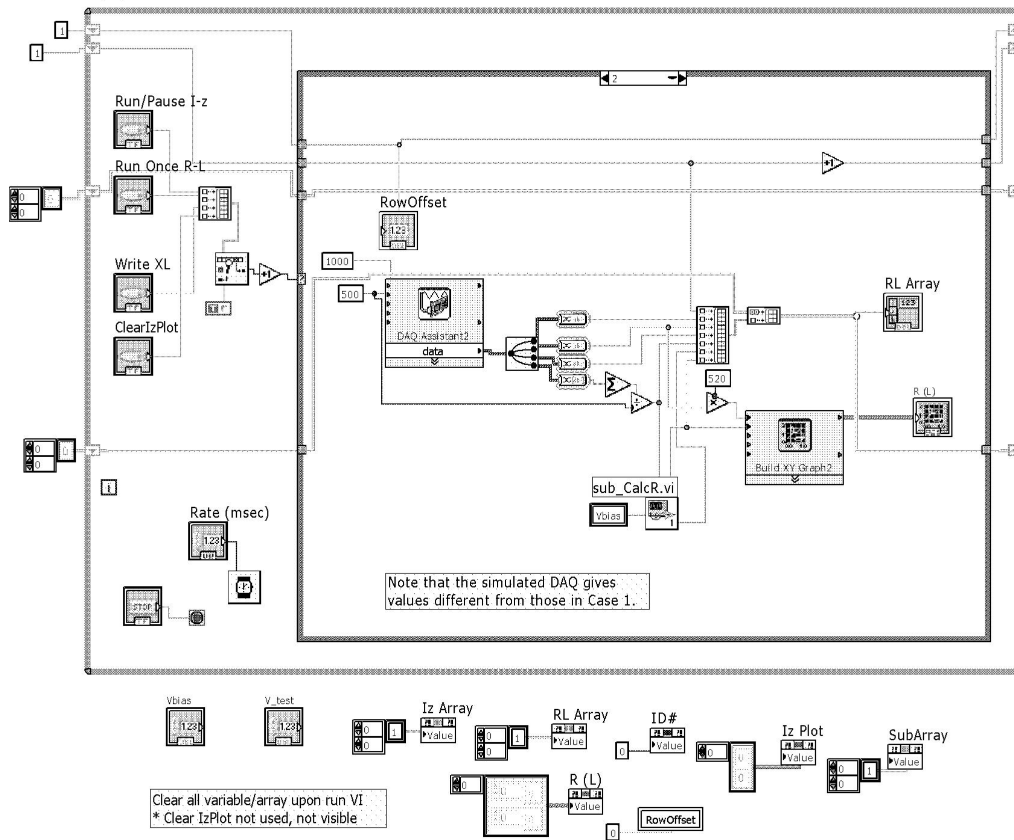

FIG. 5. 20. Block diagram of the VI from Figure 5.18.

6

SCANNING FIELD EMISSION IMAGING

Special difficulties in tip handling arose in the course of this project. Exchanging tips required 2 hours per tip with an additional bake-out of the side chamber. Finding NWs partially exposed under the film without damaging the tip also was difficult. To overcome these difficulties, a scanning field emission (SFE) method was developed. In SFE mode, the tip is pulled "far" (>10nm) from the surface with a large bias voltage (~50 V) applied. This gives the advantage of being relatively robust against crashes, allowing for longer use of each tip. This method can also be used to image semi-insulating surfaces such as oxidized silicon. We have explored the SFE method for both positive sample bias (e- from the tip) and negative sample bias (e- from the sample). The negative bias case presents high resolution with low noise, unlike with positive bias. In addition, atomic steps on a Si surface with native oxide were resolved with negative bias. We have developed an electrostatic model to explain the lateral resolution and the bias vs the gap data, at fixed tunnel current ("bias curves"). Fits to these curves give a direct determination of the local tip radius, which is found to be 5nm. This gives an expected lateral resolution of ~1nm for negative bias, which is consistent with SFE images.

6.1 Field Emission Process

The band diagram and associated field map for STM operation with typical conditions (gap g=0.5nm, Vb=1V, I=1nA, g < R radius of curvature of tip) are shown in Figure 6.1a and 1b. Bias voltage is applied to the sample with the tip

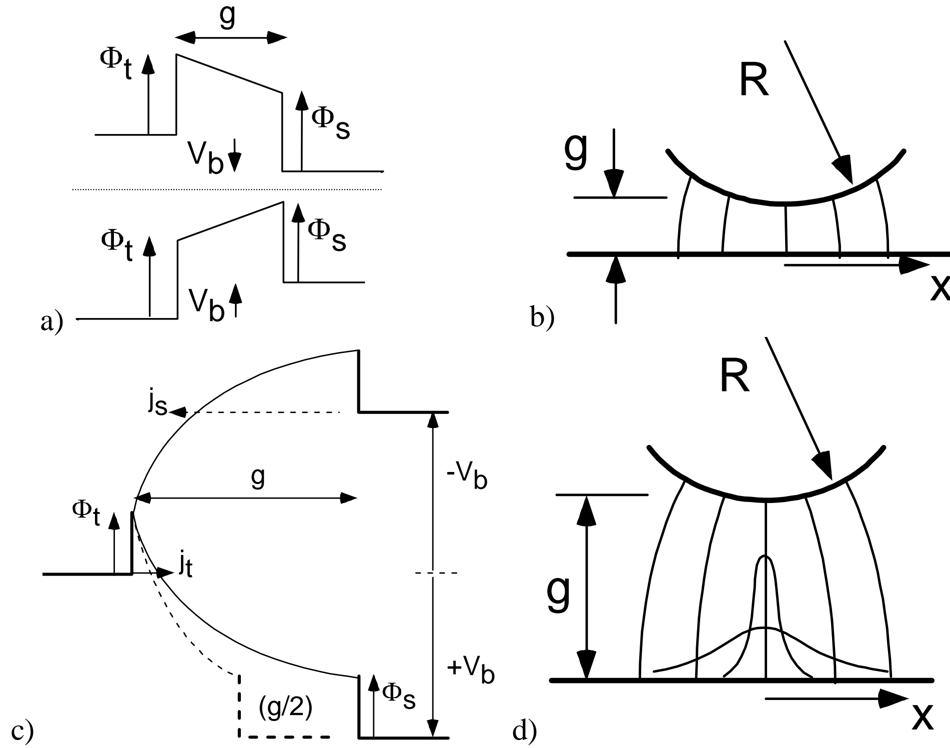

FIG. 6. 1. (a) Band diagram and (b) field map for STM operation under normal conditions (g=0.5nm, Vb=1V, I=1nA, and g<R). (c) Band diagram and (d) field map for STM operation under field emission conditions (g>R and V>Φ).

held at virtual ground at the input of the preamplifier, as is commonly done. For simplicity, both the tip and the sample are shown as metals, with equal work functions, $\Phi_{tip} = \Phi_{samp}$ ~ 4.5eV. The potential profile V(z) between the tip-sample gap, g, has a trapezoidal shape. The current results as electrons near the Fermi level of the tip, for a positive sample bias, tunnel through the barrier into empty states of the sample. For a negative sample bias the electrons come from near the Fermi level in the sample and tunnel to empty states in the tip. If the tip and sample are made of the same material, the tunneling behavior for this configuration is completely symmetric with respect to bias polarity.

The tunnel current I_{STM} is given in the WKB approximation as

$$I_{STM} \propto \exp(-2Kg), \qquad \text{(Eq. 6.1)}$$

where K=ik, and

$$\frac{(\hbar k)^2}{2m} = (E - V) \sim \langle \Phi \rangle . \qquad \text{(Eq. 6.2)}$$

Here <Φ> is the average work function of the metals, and k is imaginary for the entire path. Notice, for typical parameters $\frac{d(\ln I)}{dg} = -2k \approx 20nm^{-1}$, hence, I(g) drops by a factor 1/e for a gap increase of 0.05nm. It is this sharp dependence of I(g) on g that leads to the good lateral resolution of the STM (and provides strong feedback for the gap height in the topographic mode). The lateral resolution in the STM mode is estimated from the shape of the gap, g(x). For a spherical tip, with radius R, we have $g(x) \sim g_0 + x^2/2R$, which, for R=10nm, results in a lateral resolution of

$$\Delta x_{STM} \sim (0.2R)^{1/2} \sim 1nm . \qquad \text{(Eq. 6.3)}$$

This is different for the field emission (FE) operation, for g > R and V > Φ. The band diagram and associated field map for FE are shown in Figure 6.1c and d. As displayed, k is real for most of the path of the electrons. In this mode, the field is distinctly asymmetrical with respect to the electrodes, with the approximate values at the electrodes given by

$$F_{tip} \sim \frac{V}{R}\left[1 + \frac{R^2}{(2g - R)^2}\right], \text{ and } F_{samp} \sim V\frac{2R}{(g + R)^2} . \qquad \text{(Eq. 6.4)}$$

We note that F_{tip} is relatively strong and nearly independent of g, while F_{samp} is relatively weak and it varies approximately as $1/g^2$. The tunnel barrier at the tip (for positive bias) is relatively narrow, while the tunnel barrier at the sample (for negative bias) is relatively broad. The current-voltage behavior is highly asymmetrical.

6.2 Lateral Resolution and Analytic Model

The lateral resolution in the FE mode is also asymmetrical with respect to bias. For the positive bias, Δx is determined by the tip size R convolved with the broadening a result of electron trajectories, as they travel from the tip to the sample. Saenz and Garcia [54], expanding earlier work by Russel [55], have developed an approximate result for this case as

$$\Delta x_{FE+} \approx \sqrt{(R+g)g} \ . \qquad \text{(Eq. 6.5)}$$

For negative bias, Δx is determined by the shape of the field at the sample surface. For the point charge plus an image model, this is

$$F_{samp}(x) = F_0\left(1 + x^2/g^2\right)^{-3/2}, \qquad \text{(Eq. 6.6)}$$

where F_0 is the field at the gap center. The direction of F(x) is normal to the surface everywhere. The current density, as before, is given by the Fowler Nordheim expression [56]

$$J_{FN} = \frac{C_1}{\alpha^2}\left(\mu/\Phi\right)^{3/2} F^2 \exp\left(-C_2\Phi^{3/2}\alpha/F\right), \qquad \text{(Eq. 5.1)}$$

where J(Amp/area) is the current density, α is the correction factor for the image potential effects (near unity for this situation), μ(eV) is the chemical potential,

Φ(eV) is the work function, F(V/nm) is the field at the surface, $C_1 = 6.2 \times 10^6 A/V^2$ and $C_2 = 6.8$ V/nm-eV$^{3/2}$. We note that for typical field value, $F_0 = 1$ V/nm and g = 10 nm, $\frac{d(\ln I)}{dF} = C/F^2 \approx 65(V/nm)^{-1}$, where $C = C_2\Phi^{3/2}\alpha \sim 65V/nm$ for Φ=4.5 eV. The lateral resolution then is determined from

$$\Delta F(g) \sim F_0^2 / C = F_0\left(1 + \Delta x^2 / g^2\right)^{-3/2}, \quad \text{(Eq. 6.7)}$$

which results in

$$\Delta x \sim g(F_0 / C)^{1/2} \approx 1nm. \quad \text{(Eq. 6.8)}$$

Remarkably, this value is similar to Δx_{STM}.

6.3 Field Emission Scanning

Using the STM for field emission imaging has been attempted before, with mixed results. In most cases, the positive sample bias was used. Indeed, field emission mode was used for the "topografiner", prototype to the STM, with signal detection from the secondary electrons liberated by the field emission beam striking the sample. [57] In this instance, a lateral resolution of 400 nm was obtained. 3 nm resolution was later achieved by Fink who used FIM to obtain a single atom at the apex of a W(111) tip. [58] Kirk et al, using field evaporation to sharpen the tip to 2nm, were able to (barely) resolve atomic steps on W(110). [59] Constant current feedback was used for imaging, and the image quality was similar using either the emitted current or the secondary electrons.

Only a few groups have reported FE imaging using negative bias. [60, 61] The focus in these papers was to map the variation in work function on a

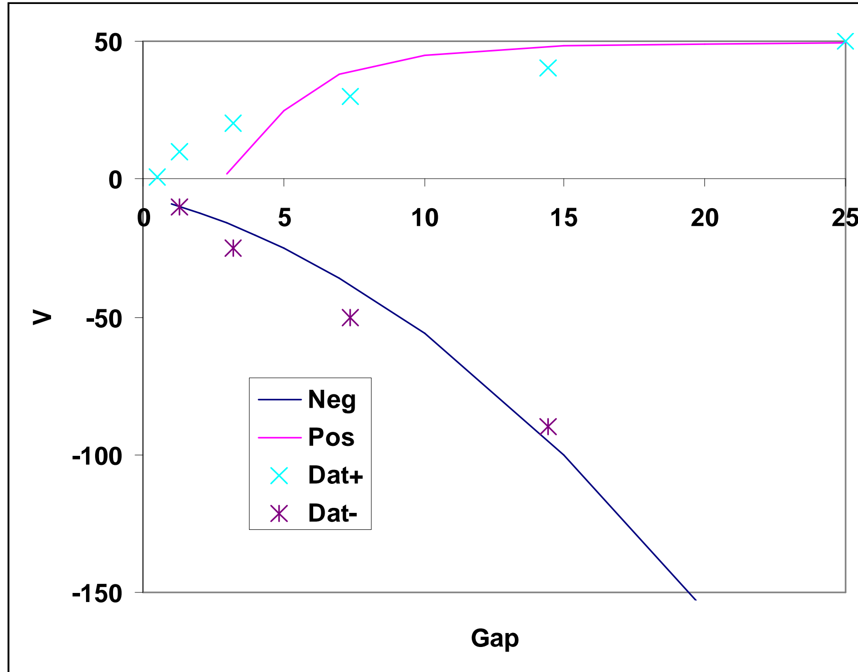

FIG. 6. 2. Gap spacing vs V_{bias} for $+V_{bias}$ and $-V_{bias}$. Analytic fits to the data are shown as solid lines with the measured data as the symbols x and * for $+V_{bias}$ and $-V_{bias}$ respectively.

heterogeneous surface, and no "high resolution" data were obtained or presented. Alternatively, Saenz and Garcia were able to resolve a monatomic step on graphite, with an approximate lateral resolution of 6nm. [54]

For STM, tunneling often occurs from a small asperity on the tip, with the local radius r smaller than the macro radius R. r can be determined experimentally by measuring a "bias curve" of V(g) at fixed I. That is, one measures the change in the gap (tip retraction) vs the bias voltage with the current fixed by feedback. A fixed origin of the gap is taken as a "tunnel point" of $g_0 = 0.5$ nm, with I = 1 nA at $V_{bias} = 1$V. Figure 6.2 is an example of a bias curve. Only the FE regime will be discussed, where G > R and the fields F_{tip} and F_{samp} are given by Eq. 6.4. First, an

analytic model is given. A numerical treatment then follows, which is necessary for fitting the data.

6.4 Bias Curve: Analytic Model

For the negative bias curve, we seek the voltage V(g) that will hold the current constant as g changes. The current is given by $I = \int j(r)dr \sim j_0 \Delta x^2$ where j_0 is from Eq. 5.1 and Δx is from Eq. 6.8. Thus, we have

$$I(g,V) = \frac{F^3}{C}\exp\left(\frac{-C}{F}\right)g^2 = I_0 . \qquad \text{(Eq. 6.9)}$$

V(g) is obtained by setting the total derivative to zero: δI=0. Since the term exp(-C/F) ~ exp(-65) dominates δI, we can simply set $F(g,V)=F_0$ (constant), to obtain the bias curve. This results for negative bias:

$$V_-(g) \big/ V_0 = \frac{(g+R)^2}{(g_0+R)^2} , \qquad \text{(Eq. 6.10)}$$

where g_0 is the gap along the center.

For the positive bias curve, in the same way, we set $F(g,V)=F_0$, to obtain

$$V_+(g) \big/ V_0 = \left[1 + \frac{R^2}{(2g-R)^2}\right]\left[1 + \frac{R^2}{(2g_0-R)^2}\right]^{-1} . \qquad \text{(Eq. 6.11)}$$

These analytic curves are plotted with the experimental data in Figure 6.2.

6.5 Bias Curve: Numeric Model

The analytic expressions for V(g) give a physical sense for the behavior, but do not fit the data very well for two reasons: Firstly, the field expressions in Eq. 6.4 require g >> R, but the data cover the range where g ~ R and below.

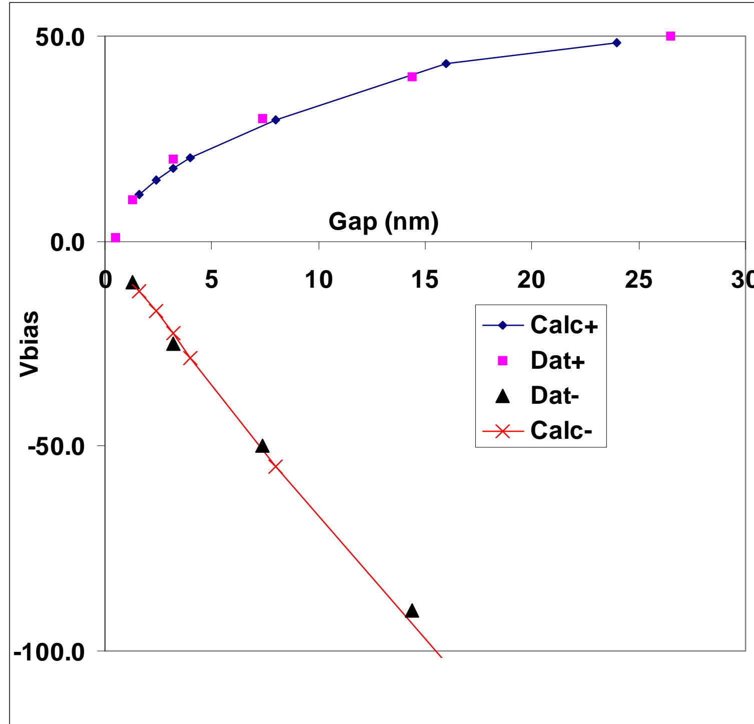

FIG. 6. 3. Gap spacing vs V_{bias} for $+V_{bias}$ and $-V_{bias}$. The numerical fits to the data are shown as connected lines with the measured data as squares and triangles for $+V_{bias}$ and $-V_{bias}$ respectively.

Secondly, the tip shape is not accurately described by an isolated sphere. A reasonable fit to the bias curves requires a numerical solution. We have done this, as displayed in Figure 6.3, with the relaxation method in cylindrical coordinates, using the Visual Basic for Applications (VBA) macros in Excel. The potential V(z,r) is a solution to the Laplace equation:

$$\nabla^2 V_{cyl}(r,\theta) = \frac{1}{r}\partial r\left(r\frac{\partial V}{\partial r}\right) + \frac{\partial^2 V}{\partial z^2} = 0\,. \qquad \text{(Eq. 6.12)}$$

For finite differences, this is written as

$$V(r,z) = \frac{1}{4}\left[V(r+\Delta r,z)+V(r-\Delta r,z)+V(r,z+\Delta z)+V(r,z-\Delta z)\right] + \frac{\Delta r}{8r}\left[V(r+\Delta r,z)-V(r-\Delta r,z)\right] \quad \text{(Eq. 6.13)}$$

Eq. 6.13 provides a recursion method for solving the Laplace equation on a grid, in which the previous value of V(r,z) is replaced by the current value of the right hand side (RHS) of Eq. 6.13. In Cartesian coordinates, the RHS is the average value of near-neighbor cells. In cylindrical coordinates, an additional "difference" term reflects the curvature of space. At the boundaries with the potential fixed (the tip and the sample), the recursion simply stops one cell short of the boundary. At the floating boundaries (the outer radius and at the top), a reflected value for the cell outside the boundary is used. Physically, this corresponds to a periodic structure in the direction of the boundary. On the centerline (r=0), the difference term vanishes by symmetry.

This algorithm was found to be stable and converge rapidly. Over-relaxation adaptations were found to be unstable and unnecessary. The VBA macro is designed to run through a set of geometries (typically, different gap values) and retain the field function along the centerline, E(0,z) for each case. Figure 6.4 displays one such tip-sample geometry. The data then can be fit by scaling the E_{tip} and E_{samp} results. That is, we seek the bias voltage, V(g), that will hold E(g) constant. Thus, we have

$$E(g) = V(g)f(g/R) = E_0, \quad \text{(Eq. 6.14)}$$

which results in

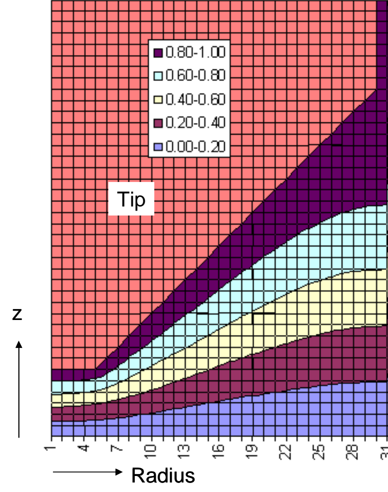

FIG. 6. 4. Contour map of potential V(r,z) in cylindrical coordinates with $V_{tip} = 1$ (conical shape) and $V_{sample} = 0$ (at z = 0).

$$V(g) = \frac{E_0}{f(g/R)}, \quad \text{(Eq. 6.15)}$$

where f(g/R) is the dimensionless field on the grid. The dimensional scale factor (nm/grid) is then applied to match the data. For the case displayed, the data are fit with a tip shape that is a truncated cone with end-radius r=6 nm and shaft angle 1/5. Note that the local radius r = 6nm is much smaller than the macro radius R ~ 250 nm obtained from V_{FET}.

The performance of the FE imaging is apparent from the images of Si (111) displayed in Figures 6.5 and 6.6. The images at 1V correspond to normal STM images. Here, the monatomic steps are clearly visible with high resolution. For positive bias, the lateral resolution degrades considerably for V > +50 V, where the gap quickly approaches 30 nm. For the negative bias images, the resolution remains excellent up to -50 V, where the gap is 7 nm. The steps remain visible,

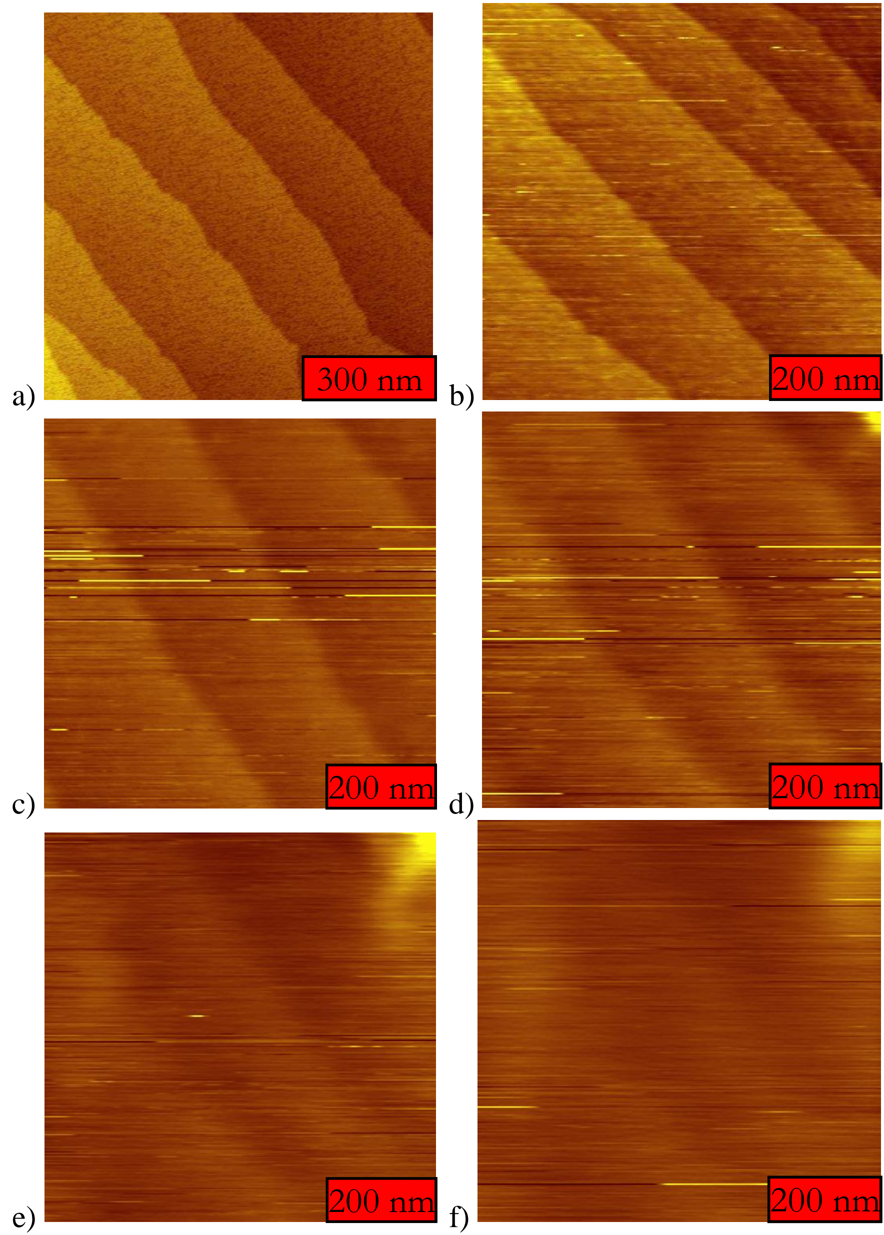

FIG. 6. 5. The SFE images of steps on Si (111) for V_{bias} equals (a) +1V, (b) +10V, (c) +20V, (d) +30V, (e) +40V, and (f) +50V. The same area is imaged for (b)-(f).

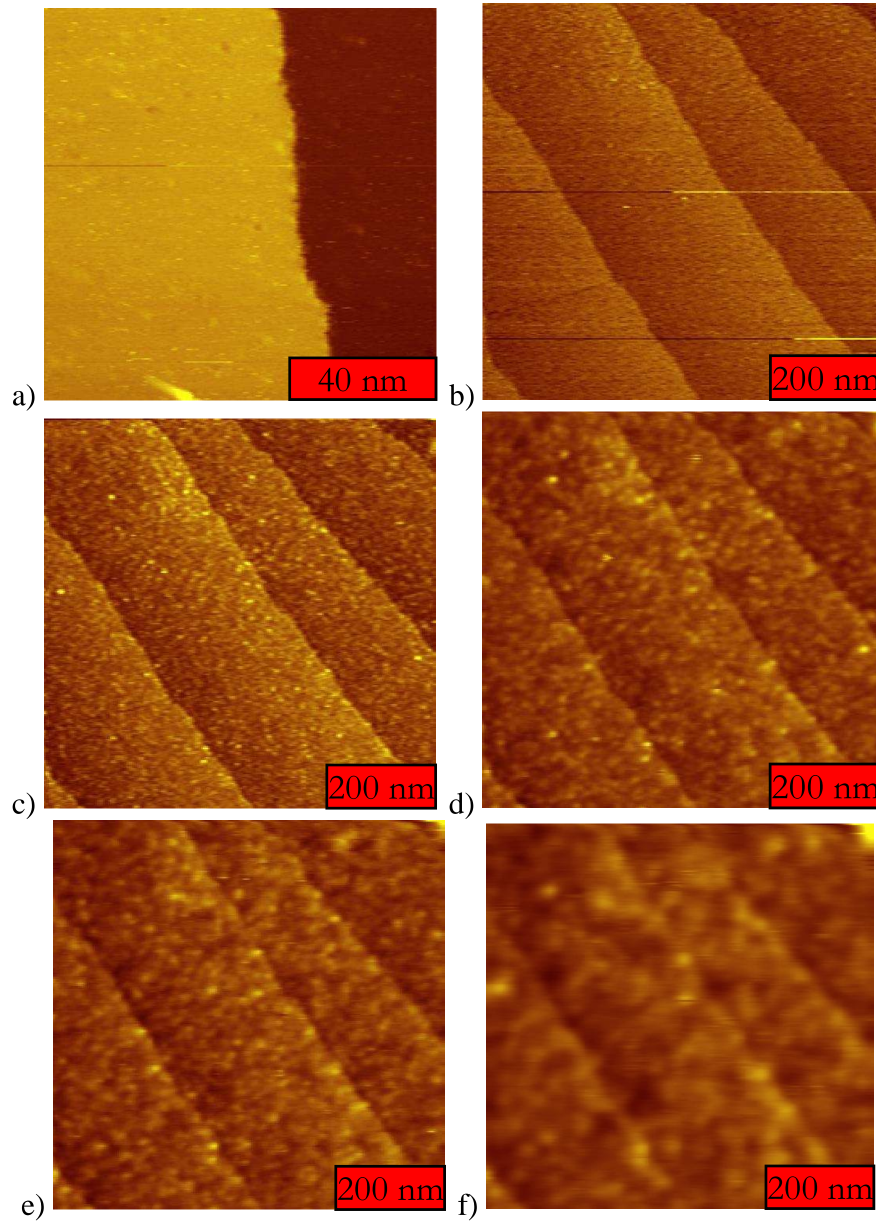

FIG. 6. 6. The SFE images of steps on Si (111) for V_{bias} equals (a) -1V, (b) -10V, (c) -20V, (d) -40V, (e) -50V, and (f) -100V. The same area is imaged for (b)-(f).

including at -100 V bias, where the gap is only 15 nm. In the negative bias images, a few small bright features are visible at random locations. These are real image features, which we attribute to adsorbed molecules.

The line scans that display the width of an atomic step are displayed in Figure 6.7. Each line is offset for ease of comparison. With the increased V_{bias}, and the increased gap, broadening of the atomic step is clearly displayed.

6.6 Noise

The positive bias images at the larger voltages present excess noise features, which we attribute to the instabilities at the surface of the STM tip. This noise does not occur for the negative bias images. We have measured the noise behavior at 50V for each polarity, as displayed in Figure 6.8. The line scan in Figure 6.8a displays the tip height at the constant current (I = 0.5 nA). The positive bias curve displays the random noise δz_{rms} ~ 0.05 nm as well as step-jumps that are characteristic of the FE instabilities. Such step jumps are very hard to "filter out". The negative bias curve displays an oscillation due to the harmonics of 60Hz, but a small noise of $\delta z_{rms} < 0.01$ nm. The noise behavior is better presented in the spectral plot displayed in Figure 6.8b. The noise density in the negative bias is nearly 100 times smaller for the positive bias, at frequencies below the feedback response. The 60 Hz and the harmonics are apparent in the spectral plots.

6.7 Images of Oxidized Silicon

The SFE imaging can also be done on the samples with oxide layers. With the gap size significantly larger, a thin insulating oxide layer can be penetrated

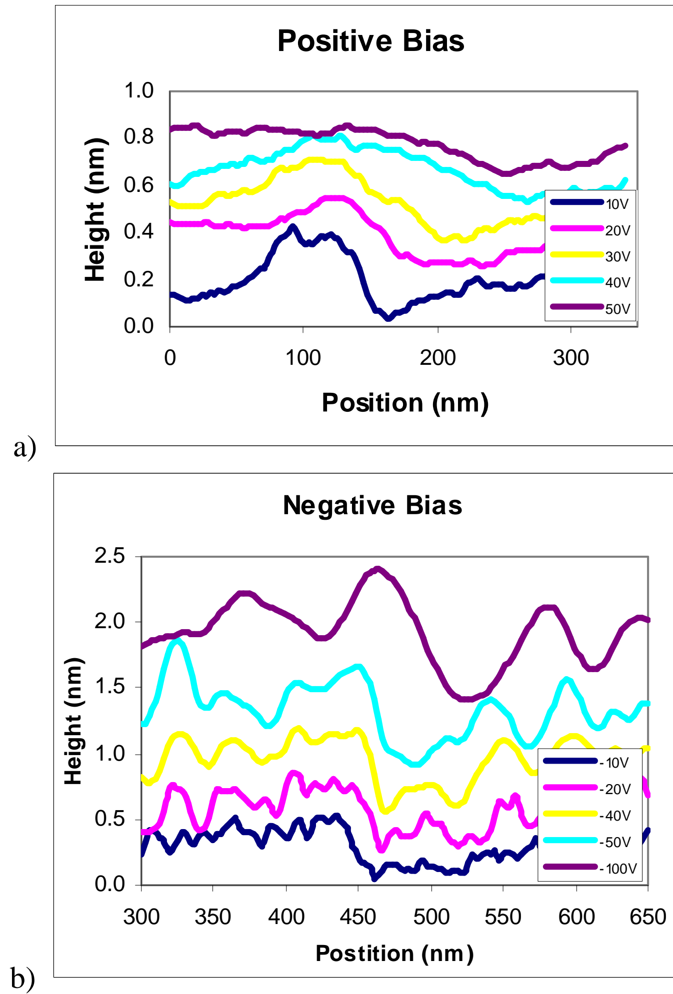

FIG. 6. 7. The line scans over a step for field emission images for (a) $+V_{bias}$ and (b) $-V_{bias}$. The higher V_{bias} line scans are offset for easier comparison. The lower lateral resolution is evident in the larger V_{bias} line scans by the broadening of the atomic step.

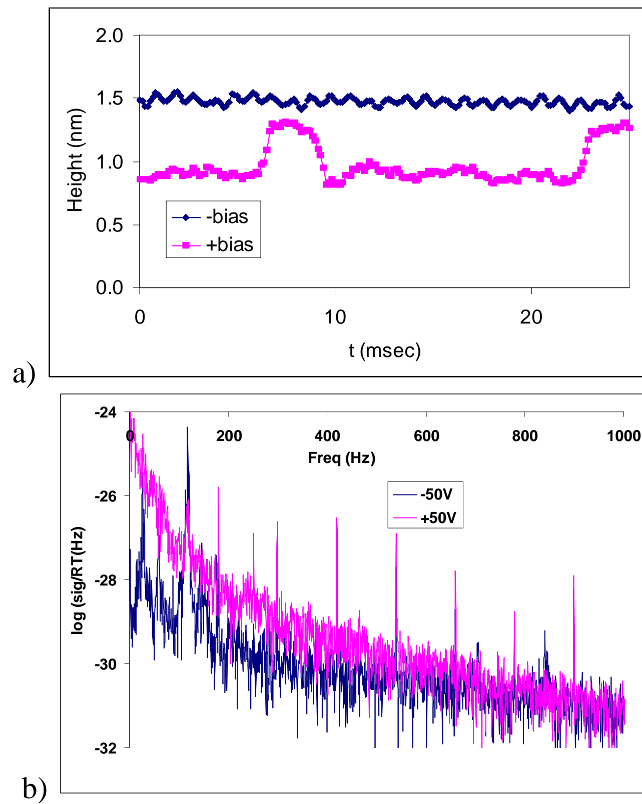

FIG. 6. 8. Noise plots for V_{bias} = -50V and +50V. (a) Line scan of the 'noise' image. For $+V_{bias}$ the step-jump occurs twice within the 25ms. The $-V_{bias}$ noise levels are mainly the 60 Hz harmonic oscillations. (b) Frequency vs log(Signal) for both $+V_{bias}$ and $-V_{bias}$. $+V_{bias}$ noise is 100 times larger for f < 100 Hz.

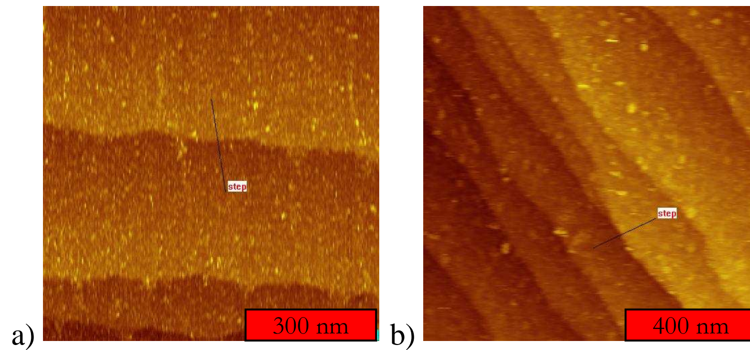

FIG. 6. 9. The SFE images of the atomic steps under oxide with thicknesses of (a) 2.3 nm and (b) 3.1 nm on Si (111). V_{bias} = -10 V.

without damaging the tip. The scans were completed on the samples with oxides 2.3 nm and 3.1 nm thick. Ellipsometry was used to check the oxide thicknesses. Figure 6.9 displays the atomic steps evident on oxidized Si (111). STM images were also attempted but resulted in crashing of the tip with no visible image. The samples exposed to air for long periods of time (> 1 month) were also scanned with the SFE. $CoSi_2$ NWs, Figure 6.10, were imaged after 1 month of air exposure with V_{bias} = -10 V.

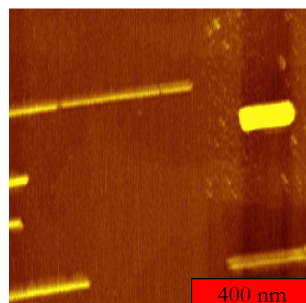

FIG. 6. 10. SFE images $CoSi_2$ NWs on Si (110) after sample sat in air for 1 month. V_{bias} = -10V.

7

PLATINUM / SILICON (100) NANOWIRES: GROWTH

7.1 Introduction

Platinum (Pt) silicide NWs offer many potential electronic device applications. It makes structures with low oxidation rates in atmospheric environments. [37] Pt interconnects have been studied for non-volatile memory technologies. [15] This has led to the study of its resistivity. [62] As part of this dissertation, a further understanding of how PtSi NWs grow on Si (100) is given.

7.2 PtSi Nanowires

Platinum Silicide (PtSi) NWs were formed by depositing ~1 ML Pt on heated Si (100) in UHV. The surface of Si (100) produces two domains for NWs, which are orientated perpendicular to each other. There is debate as to whether the structure of the silicide is PtSi or Pt_2Si. [37, 63] This project does not seek to resolve that debate. Instead, NW structural characteristics are investigated. The images were taken by STM and AFM. Figure 7.1 shows scans taken with the growth temperatures of 600, 700, 750, and 800°C.

When Pt was added at 600°C, the resulting silicides formed 2 basic shapes: NWs and rectangular islands, as displayed in Figure 7.1a. The majority of the Pt, over 70%, went to making the islands. The remaining Pt formed NWs with average width of 10 nm and average length of 50 nm.

At 700°C, NWs dominated the silicide structures, as displayed in Figure 7.1b. A dual mode structure was observed. Smaller NWs, with widths ~ 10 nm, were still present and dominated the image. The larger NWs, with widths ~ 30 nm,

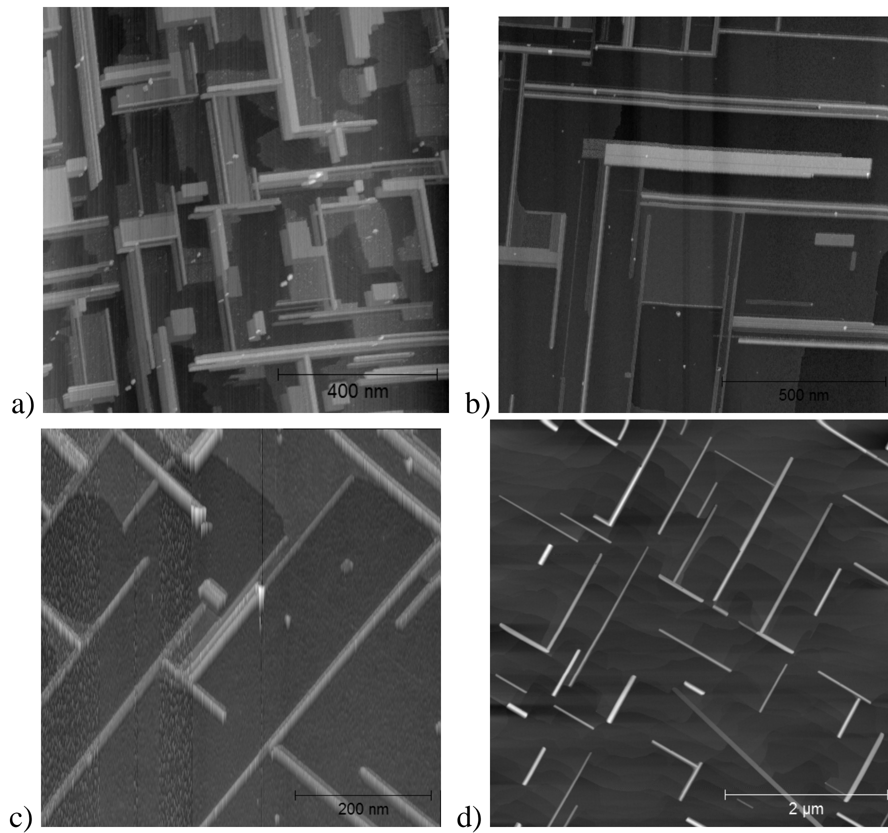

FIG. 7. 1. AFM images of PtSi nanowires on Si (100) (a) 600°C, (b) 700°C, (c) 750°C, and (d) 800°C growth temperatures. The NWs grow progressively larger and less dense with the increasing T.

grew as well, taking the bulk of the Pt deposited (> 55%). Both of the NW structures grew to similar lengths of 800 nm.

The dual mode displayed at 700°C is replaced with the single mode of the NWs when 750°C is used for the growth temperature, as displayed in Figure 7.1c. Large NWs, widths ~ 35 nm, are discovered to grow to 1000 nm in length. Similar NWs were observed at the growth temperature of 800°C, as displayed in Figure 7.1d. These NWs are slightly larger with width ~ 40 nm and length of ~ 1300 nm. Table 7.1 displays the lengths and the widths of PtSi NWs for various growth temperatures.

We did not measure the resistivity of PtSi NWs. The custom sample preparation chamber had not yet been put together and the contact pad materials were unstable beyond a few days. This led to changing materials for NW growth to cobalt and iron, with titanium as the contact pad. When the titanium contact pad was found to be stable for long periods of time, the study of iron silicide NWs was deep underway, as discussed later. Other projects and goals prevented returning to the Pt system.

Lim et al measured resistivity of $PtSi_2$ NWs on Si (100). [62] They were grown at 650°C and measured with a variable-spacing dual STM tip system. They found $\rho = 13.7 \pm 2.4$ μΩ cm with $\sqrt{A} = 2.6$ nm. It is unclear if these NWs are the same silicide structures as those studied in our project.

T (°C)	NW ave. length (nm)	NW ave. width (nm)	Comments
600	50	10	Dual Mode: NW and square islands
700	800	10 and 30	Dual Mode: 2 different sized NWs
750	1000	35	Single Mode
800	1300	40	Single Mode

TABLE 7. 1. PtSi NWs on Si (100) at various T in UHV.

8

IRON / SILICON (110) NANOWIRES: RESISTIVITY

8.1 Iron Silicide Compounds

Iron silicide alloys display a rich variety of structural, electronic and magnetic behavior. For example, the β-$FeSi_2$ phase is semiconducting, and has possible applications in fiber-optic communications or photovoltaics. [64-66] FeSi is a paramagnetic semiconductor, or Kondo insulator. [67] Fe_3Si is a Heusler alloy, with a high Curie temperature of 840K and is fully spin polarized. [68] The structural and electronic properties of the thin films of iron silicide grown by MBE depend sensitively on stoichiometry and strain. [69, 70] During the initial stages of deposition of Fe on Si in UHV, a variety of meta-stable phases occur, some with ferromagnetic ordering. [71] High quality, buried layers of $FeSi_2$ can be formed by ion implantation and annealing. [72] There are some of the Fe-Si phases that can be formed as NWs, including FeSi formed by CVD, [73, 74] Fe_3Si formed by a metal-enrichment diffusion reaction[75] and $FeSi_2$ formed by endotaxial growth. [28-30, 76, 77]

8.2 Nanowires

$FeSi_2$ NWs were formed by depositing ~ 1 ML Fe onto a heated Si (110) substrate in UHV. The substrate orientation results in a single orientation domain, so the NW length is not limited by collision with other NWs. We previously determined that the NWs formed under these conditions are $FeSi_2$, though the phase was not unambiguously assigned between α-(tetragonal), γ-(fcc) or s-(bcc). [77] Fe was supplied by sublimation from a 5N-purity Fe wire.

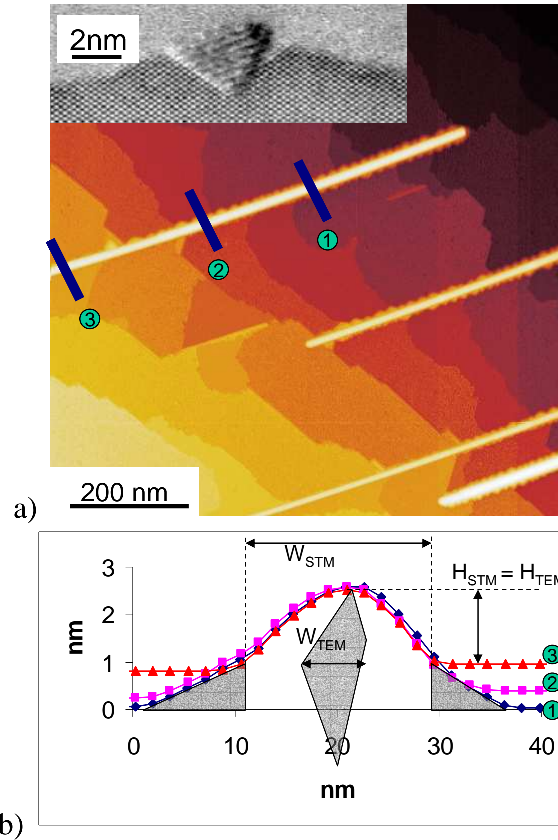

FIG. 8. 2. (a) FeSi2 NWs on Si (110). Cross-section TEM image (inset) displaying bunched Si around NW. There are linescans overlapped in (b) also displaying Si steps bunching together around NW. The width of NW convoluted from STM tip.

8.3 Determination of Cross Sectional Area

To obtain ρ from equation 4.4, the cross-sectional area A of the NW must be determined. This measurement is difficult because the NWs are embedded into the substrate, and because the NW width is comparable to the local radius of the STM tip. A sample image with several NWs is shown in Figure 8.1. Our procedure for determining area was to use the STM-measured height of the NWs above the surface, combined with the known cross-sectional shape determined

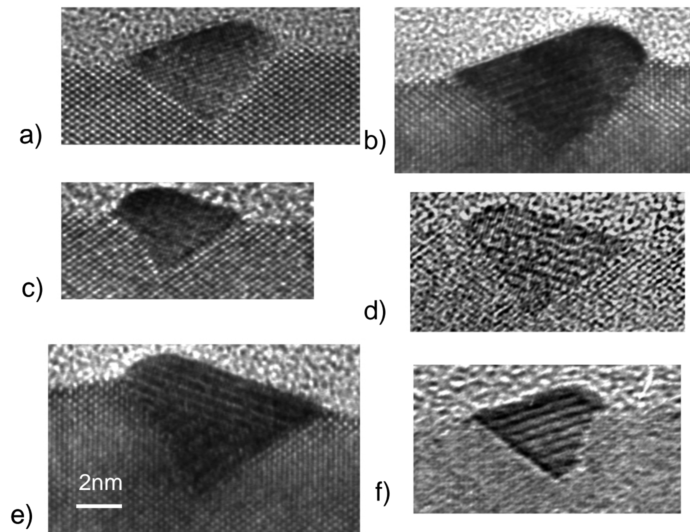

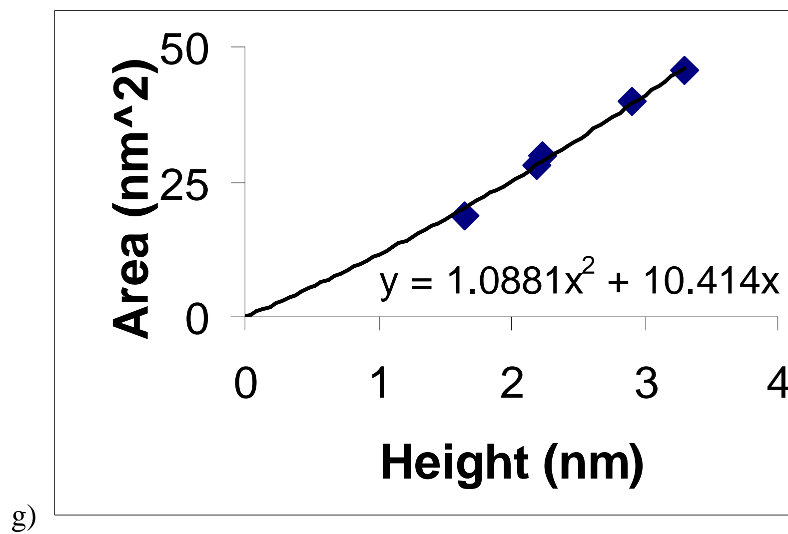

FIG. 8. 3. (a)-(f) Cross section TEM images of FeSi2 NWs on Si (110). Scale in (e) is used for all images. (g) Height above surface vs Area as determined by (a)-(f) with corresponding fit curve.

from the high-resolution TEM images, displayed in Figure 8.2a - f. In particular, from a representative set of TEM images from various NWs, we found an invariant, asymmetrical shape with

$$A(nm^2) = 1.1H^2 + 10H \ , \qquad \text{(Eq. 8.1)}$$

where H (nm) is the height above the surface. This relationship is displayed in Figure 8.2g. The measurement of height is not affected by the tip resolution, which may degrade somewhat after multiple contacts. The STM-measured width, however, varied with the condition of the tip, and was typically 5-10 nm larger than the physical width determined from TEM. Due to the asymmetrical shape of the NW cross-section, we characterize the NW size as √A. The uncertainty in √A was estimated from ΔH ~ 0.19 nm (one atomic layer). This yields an uncertainty of ~15% in √A and of 30% in ρ for √A ~ 4nm. The size of the 6 NWs visible in Figure 8.1 ranges from 1 to 5 nm.

Because the substrate was stepped in the long direction of the NW, a subtle point arose regarding the height measurement: The NWs do not cross step edges, as discussed previously, the steps are pushed inwards at one end of the NW and outwards at the other end. Further evidence of this behavior is seen in Figure 8.1. This image has been leveled with respect to the top surface of the NW, which is parallel with Si (110) planes. The surrounding surface drops away in the downhill direction in monolayer steps (ΔH ~ 0.19nm). If instead the image were leveled across the terraces, the NW would appear to be tapered due to saturation of the grey scale. The height measurement should be made on the terrace upon

which the NW began growing. This terrace was usually apparent from the step-flow pattern and usually occurred near the middle of the NW. Alternatively, the NW height can sometimes be determined from the shape of a linescan across the step-down end of the NW, if the linescan displayed a well-defined silicide facet on top of a broader shoulder. An example is displayed in Figure 8.1b. In this case, H can be measured from the base of the facet. The broad shoulder below the facet consists of step bunches adjoining the NW. This shoulder often displayed an angular rumpled structure along the NW sides, as seen in the STM image of Figure 8.1a. The same shoulder is sometimes visible in cross-section TEM images, such as in Figure 8.1a inset.

8.4 Resistance vs Distance Data

In Figure 8.3a, there are three NWs visible, which lie across, under and away from the contact edge. They are labeled NW1, NW2 and NW3, respectively. The contact pad is visible within the STM topographic image in the form of extra "noise" on the region of the contact. It may also be discerned from a height increase across the edge. A dotted line marks the edge of the contact pad in the figure. The edge is best defined by the resistance profile R(x) running parallel but offset from a NW, as displayed in the inset of Figure 8.3d. The resistance values along this path ranged from $R = 10^3$ to 10^{10} ohms. This gives evidence of the Schottky barrier for W/Si of the tip-substrate system. For the purpose of R(L) measurements, the width of the contact pad edge may be defined as the range over which R_{pad} changes from 0.1 R_{NW} to $10R_{NW}$. This corresponds to a width of 20 nm, in this example. NW1 straddles the contact edge and is suitable for R(L)

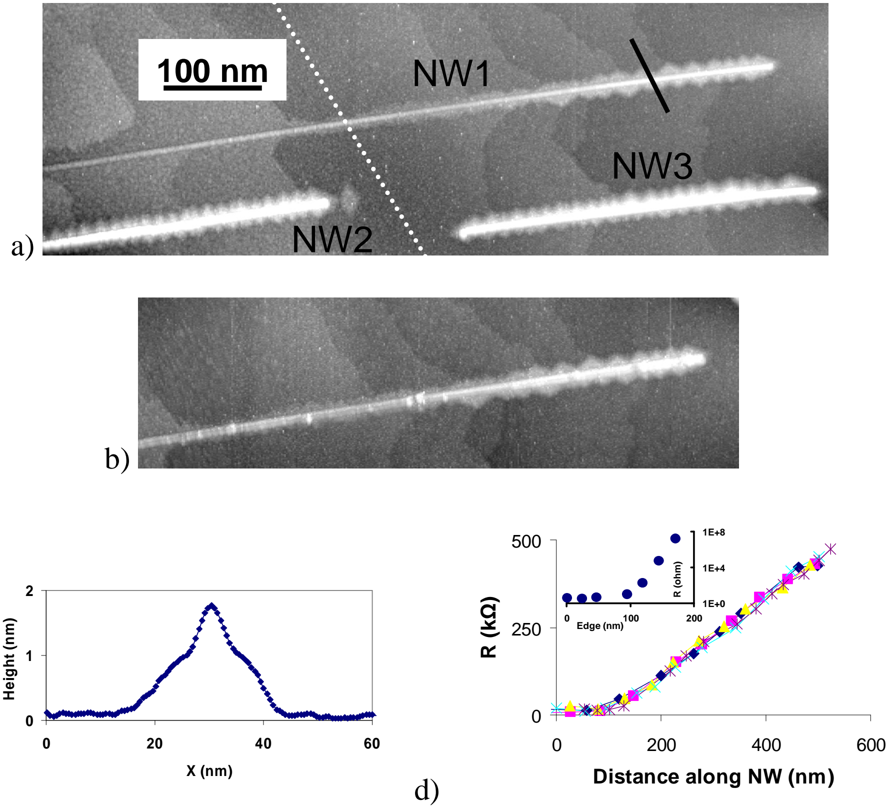

FIG. 8. 4. (a) Three NWs laying across (NW1), under (NW2), and away (NW3) from Ti contact pad, displayed as a dotted line. (b) NW1 after many contacts for measurements displaying minimal damage. (c) Linescan on NW1 displaying height above bunched Si. (d) R vs L curve along NW1 with R vs L parallel to NW1 for contact pad formation (inset).

measurements. NW3 is well removed from the contact edge. Its resistance through the Schottky barrier of NW/Si was $R_B \sim 10^6$ ohms.

Figure 8.3d shows the R(L) values obtained for NW1. Five separate "runs" are shown, with bias ranging from 2-10 mV, and with the tip stepping either towards or away from the contact edge. These curves overlap within their uncertainties, which shows that the multiple contacts did not disturb the NW resistances. The STM image (Figure 8.3b) taken after the set of electrical measurements shows a few small features at some of the contact points along the NW. Most of the contact points were "invisible". The slope of the R(L) data, in the region beyond 100nm, is $dR/dL = 1090 \pm 80\ \Omega/\text{nm}$. The region below L = 100nm was excluded from the fit, because the trend is curved due to the finite electrical width of the contact edge. We note that the zero for the distance scale, L_0, is arbitrary. Since ρ is determined from dR/dL we do not concern ourselves with L_0 which is related to R_c.

To determine area, the height is needed for NW1. The cross section displayed in Figure 8.3c presents the bunched steps below the prominent NW on top. For NW1, $H = 0.6 \pm 0.1$ nm giving $A = 6.6 \pm 2.0\ \text{nm}^2$ and $\rho = 505 \pm 150\ \mu\Omega$ cm.

8.5 ρ vs Size Data

Figure 8.4 shows ρ vs $\sqrt{A}$ for a set of 22 NWs on three samples grown at temperatures spanning 700°C to 800°C in order to produce a range of sizes. Error bars are indicated for representative points, and are dominated by NW size, which

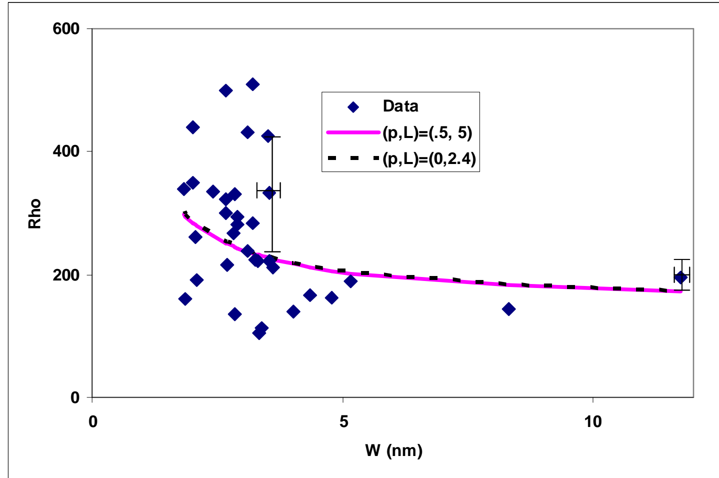

FIG. 8. 5. ρ vs √A for 22 NWs on 3 samples ranging T = 700 – 800°C. Two Fuchs – Sondheimer fits are shown for p = 0.5 (solid line) and 0 (dashed line) and ρ_0 = 150 μΩ cm. λ values are found to be 5 and 2.4 nm respectively.

affects both axis. Uncertainty in the NW size is dominated by a height uncertainty of ±1 ML, which contributes a larger fraction for smaller NWs.

Note that these endotaxial NWs are single-crystal structures so a fit to the FS equation, equation 2.12, is the only fit we are using. The fitting parameters ρ_0, λ and p are strongly coupled such that unique values cannot be assigned, given the large uncertainties in the data. We have fixed ρ_0 = 150 μΩ cm to match the larger NWs, which have relatively small uncertainties, and for which size effects are expected to be small. λ and p remain strongly coupled. Two equivalent pairs are displayed in Figure 8.4. For discussion, we will fix p and fit λ. Earlier work on epitaxial thin films of $CoSi_2$ on Si(111) suggests p ~ 1 for a good silicide film. [11] This would produce zero size dependence (flat line), which clearly does not fit the data. On the other extreme, p = 0 corresponds to fully inelastic scattering at the

boundary. This seems unreasonable in view of the structural perfection of the self-assembled, single-crystal structures. Fixing p = 0.5, then, we obtain a fit value of λ = 5.0 nm $\pm$ 50%. The uncertainty is determined by curves that include 2/3 of the data points.

The measured value of ρ_0 ~ 150 uΩ cm is close to the bulk value of ρ_{bulk} = 250 uΩ cm reported for single-crystal α-$FeSi_2$. [9] Similar values are reported for 100 nm buried films of α-$FeSi_2$ fabricated with ion beam synthesis. [72, 78] We point out that the actual phase for the $FeSi_2$ NW structure is not unambiguous between α-, s- or γ-phase. The resistivity values are not available in the literature for the latter two. The ex situ measurements of endotaxial $FeSi_2$ NWs using lithographically defined contact pads reported $\rho > 10^3$ uΩ cm. [79] This large value was attributed to uncontrolled contact resistance, and the possible damage to the NWs during fabrication. Ex situ measurements of oxidized endotaxial $FeSi_2$ NWs at 300K using conducting-tip AFM reported ρ ~ 150 uΩ cm for $\sqrt{A}$ ~ 30 nm. [76] No explanation was given for the smaller-than-bulk value, and the contact resistance was uncharacterized.

8.6 Temperature and Surface Oxide Effects

We have also explored how ρ varies with temperature and partial oxidation of the NWs. Figure 8.5a displays R(L) for $\sqrt{A}$ = 2.9 nm, measured at 300K and also at 130K. This required tracking the sample position during cool-down, which caused a drift of ~ 1 um. A two-temperature measurement enhances the sensitivity to temperature effects by removing the statistical uncertainty in

NW size. The result for this NW was dR/dL = 1.80 ± 0.1 and 1.3 ± 0.3 kΩ/nm at 300K and 130K, respectively. The decline of 20 – 30 % upon cooling is consistent within uncertainties with the temperature effect reported for bulk single-crystal α-$FeSi_2$: ρ = 250 vs 230 uΩ cm at 300K vs. 4.2K. [9] Figure 8.5b shows R(L) for √A = 3.2 nm following exposure to air for 20 min. In this case, it is not possible to compare the same NW before/after oxidation, of course, so ρ includes the uncertainty in √A. The measured resistivity for the oxidized NW was ρ = 280 ± 100 uΩ cm. It is indistinguishable from the un-oxidized NWs of the same size.

The relatively small value of λ = 2.4 nm obtained for the $FeSi_2$ NWs is consistent with the relatively high value of bulk resistivity, ρ_0 = 150 μΩ cm. ρ and λ are independent parameters in the FS model. They are physically coupled in the Sommerfeld model. Using equation 2.11, with an estimated carrier density of n ~ 3×10^{22} cm^{-3} (as for $CoSi_2$), the implied scattering length is λ = 0.5 nm. This value is smaller than that measured for the NWs, which may be either due to a poor estimate for n, or due to the simple nature of the Sommerfeld model. The measured value has reasonable physical meaning, since the parameter √A is explicitly varied in the experiment. In either case, the small value of λ may reasonably be attributed to lattice vacancies in the NW structure. Indeed, α-$Fe_{1-x}Si_2$ is a non-stoichiometric crystal with vacancies on the Fe sub-lattice. [80] For x = 0.2, the mean distance between vacancies is 0.4 nm. The large value for bulk resistivity due to intrinsic structural defects is familiar for other materials. It is known as a "saturation resistivity" in ρ(T) experiments. [81] For example,

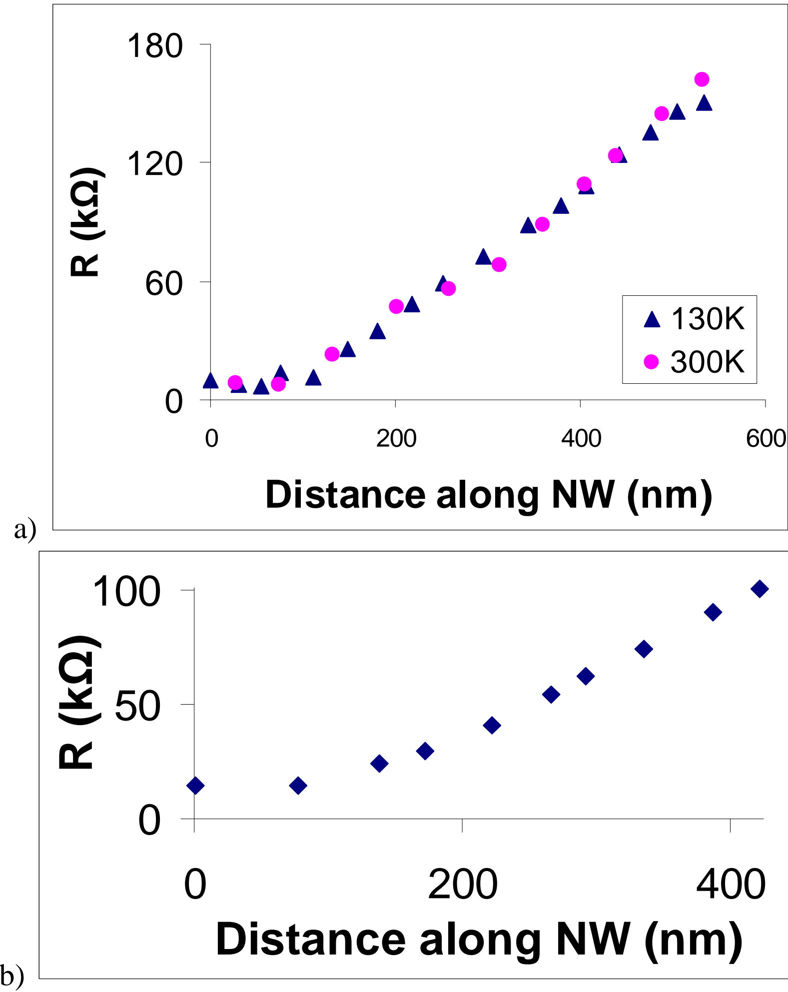

FIG. 8. 6. (a) R(L) curve for NW measured at T = 300K and 130K. dR/dL = 1.80 ± 0.1 kΩ/nm and 1.3 ± 0.3 kΩ/nm respectively (b) R(L) curve for air exposed NW. ρ = 280 ± 100 μΩ cm for √A = 3.2 nm.

CoSi has ρ_0 = 274 $\mu\Omega$ cm, with corresponding inferred λ = 0.2nm. In this sense, the value λ = 5.0 nm obtained from the FS fit is surprisingly large. The observed insensitivity of ρ to cooling from 300K is expected, since the phonon scattering length of 40 nm at 300K is much larger than λ from structural defects, hence the latter dominates.

From the materials science viewpoint, the inferred invariance of vacancy concentration vs. NW size is surprising. If the vacancies are stabilized by entropy at the growth temperature (700°C), one would expect them to easily diffuse 1 nm to the free surface and disappear during cool-down to 300K. Alternatively, if the vacancies are in equilibrium at 300K, one might expect that strain in sub-10 nm structures would alter this concentration, either upwards or downwards, compared with unstrained bulk values. Effects of this type can dominate the kinetics and energetics of self-assembled nanostructures, as in the example of hollow nanoparticles formed via Kirkendall voids. [82] It is known that vacancies provide a pathway between well-defined stoichiometric compounds in thin film reactions. The resulting structures can be very sensitive to strain, as documented in the Ni-Si, Fe-Si and Co-Si systems. [83-86] Our results for the electrical conduction in $FeSi_2$ NWs indicate that the vacancy concentration in $FeSi_2$ is a robust feature, even in sub-10 nm endotaxial nano-structures.

9

SUMMARY AND FUTURE WORK

The study of silicide NWs is an ongoing process and attracts the interest of many, both in structure and application. This dissertation focused on in situ resistivity measurements of $FeSi_2$ NWs grown on Si(110) in UHV. This was made possible by the construction of a sample preparation chamber. The use of STM was predominate in imaging and essential is measuring ρ. A 2-point variable distance method was used to measure R(L) between the movable STM tip and a stationary contact pad. To prevent frequent tip crashes, a new mode of imaging was used, SFE, and presented here with an analytical and numerical model of operation.

For $FeSi_2$ NWs in the size range of 2 - 12 nm, the resistivity at room temperature is mostly independent of size and has the value $\rho_{NW} = 150 \pm 80$ uΩ cm. A fit to the size dependence below 4 nm using the FS model with parameters p = 0.5 gave λ ~ 5 nm. The resistivity is essentially unchanged upon cooling from 300K to 130K, or upon exposure of the NWs to air to induce oxidation of the surface. These results are attributed to a high equilibrium concentration of vacancies in the $FeSi_2$ structure, which corresponds to an inelastic electron scattering length of ~ 1 nm. It is remarkable that the vacancy concentration persists in very small structures, and is not changed by surface oxidation.

This information is added to ρ measurements of NWs already in circulation (Table 9.1). Figure 9.1 displays a unifying plot of size vs ρ for these

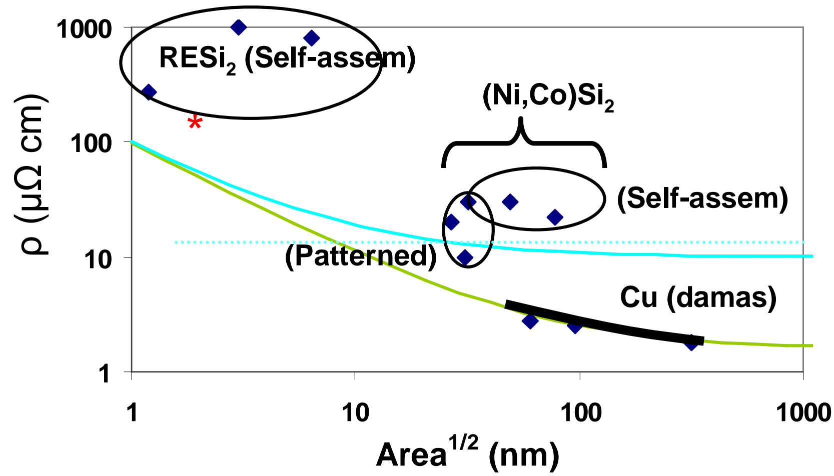

FIG. 9. 1. Plot of various NWs by √A vs ρ on the same axis. Includes all values currently published. $FeSi_2$ NWs studied in this project added as red star.

NWs. Three lines are displayed within the figure displaying various FS curves for different material: the lower solid line is Cu ($\lambda = 40$ nm, $\rho_0 = 1.6$ μΩ cm, and $p = 0$), the upper solid line is $NiSi_2$ ($\lambda = 6$ nm, $\rho_0 = 10$ μΩ cm, and $p = 0$), and the dotted line is $CoSi_2$ ($\rho_0 = 15$ μΩ cm, and $p = 1$). Information obtained in this project is added to the table and figure.

Future work involves measuring other endotaxial NW systems. Also, use of the dual domain Si (100) surface can be used to study closely spaced, but not touching, NWs for potential applications as nano-transistors. The knowledge from studying these systems can be used for furthering the advances in technology.

Material	ρ ($\mu\Omega$ cm)	ρ_0 ($\mu\Omega$ cm)	ρ/ρ_0	A (nm^2)	L (nm)	Contacts
NiSi[87]	10	10[88]	1.0	25*25	1k	EBL
$CoSi_2$/Si(110) [89]	30	15[90]	2.0	60*40	1k – 3k	4-pt STM
$ErSi_2$/Si(100) [91]	1k	30[92]	30	3*3		2-pt STM
$ErSi_2$/Si(100) [13]	800	30	25	20*2		2-pt STM
$ErSi_2$/Si(100) [93]	270	30	9	2.1*0.7	70-500	2-pt STM
Pt_2Si/Si(100) [62]	14	30 [94]	0.5	0.8*8.5	1400	2-pt STM
$CoSi_2$/Si(110) [44]	22	15	1.5	100*60	30-600	2-pt STM
Cu [14]	2.5	1.75 [14]	1.4	230*40		EBL
AuPd [95]	120	3	40	5*8	2k	4-pt STM
$FeSi_2$/Si(110)	150	240	0.6	3*2	300 – 1k	2-pt STM

TABLE 9. 1. Measured resistivity values for various metallic NWs as found in current publications. All values given at 300K. FeSi2 NWs studied in this project are added at bottom.

BIBLIOGRAPHY

1. Nahid, M.A.I., et al., *Study of Structure, Magnetic and Electrical Properties of Co2MnSi Heusler Alloy Thin Films Onto n-Si Substrates.* Ieee Transactions on Magnetics, 2009. **45**(10): p. 4030-4032.

2. Bogels, G., et al., *Morphology and growth mechanism of multiply twinned AgBr and AgCl needle crystals.* Journal of Crystal Growth, 1999. **203**(4): p. 554-563.

3. Jedema, F.J., et al., *Spin injection and spin accumulation in all-metal mesoscopic spin valves.* Physical Review B, 2003. **67**(8).

4. Hao, L. and P.A. Bennett, *Analytic model for minority carrier effects in nanoscale Schottky contacts.* Journal of Applied Physics, 2010. **108**(1): p. 014303.

5. Honda, S., et al., *Spin polarization control through resonant states in an Fe/GaAs Schottky barrier.* Physical Review B, 2008. **78**(24).

6. Kioseoglou, G., et al., *Electrical spin injection into Si: A comparison between Fe/Si Schottky and Fe/Al[sub 2]O[sub 3] tunnel contacts.* Applied Physics Letters, 2009. **94**(12): p. 122106.

7. Ando, Y., et al., *Electrical injection and detection of spin-polarized electrons in silicon through an Fe3Si/Si Schottky tunnel barrier.* Applied Physics Letters, 2009. **94**(18): p. 182105-.

8. Zeng, C.G., et al., *Charge-order fluctuations in one-dimensional silicides.* Nature Materials, 2008. **7**(7): p. 539-542.

9. Hirano, T. and M. Kaise, *ELECTRICAL RESISTIVITIES OF SINGLE-CRYSTALLINE TRANSITION-METAL DISILICIDES.* Journal of Applied Physics, 1990. **68**(2): p. 627-633.

10. Ashcroft, N.W. and N.D. Mermin, *Solid State Physics*. 1976: Thomson Learning.

11. Hensel, J.C., et al., *Specular Boundary Scattering and Elecrical Transport in Single-Crystal Thin Films of CoSi2.* Phys. Rev. Lett., 1985. **54**(16): p. 1840-3.

12. Fuchs, K., *~Boundary scattering model~.* Proc. Cambridge Phil. Soc., 1938. **34**: p. 100.

13. Zhigang, L. and e. al, *Resistivity measurements of self-assembles epitaxial grown erbium silicide nanowires.* J. Phys. D, 2006. **39**: p. 2839-42.

14. Steinhögl, W., et al., *Size-dependent resistivity of metallic wires in the mesoscopic range.* Physical Review B, 2002. **66**(7).

15. Rosezin, R., et al., *Electrical properties of Pt interconnects for passive crossbar memory arrays.* Microelectronic Engineering, 2009. **86**(11): p. 2275-2278.

16. Mayadas, A.F. and M. Shatzkes, *~Grain boundary scattering model~.* Phys.Rev., 1970. **B1**: p. 1382.

17. Steinhogl, W., et al., *Size-dependent resistivity of metallic wires in the mesoscopic range.* Physical Review B, 2002. **66**: p. 075414.

18. Henzler, M., et al., *Epitaxial insulating films.* Surface Review and Letters, 1998. **5**(3-4): p. 675-684.

19. He, Z., D. Smith, and P. Bennett, *Endotaxial Silicide Nanowires.* Physical Review Letters, 2004. **93**(25).

20. Preinesberger, C., et al., *Formation of dysprosium silicide wires on Si(001).* J. Phys. D: Appl. Phys., 1998. **31**: p. L43-45.

21. Preinesberger, C., et al., *Structure of DySi2 nanowires on Si(001).* J. Appl. Phys., 2002. **91**(3): p. 1695-7.

22. Parkin, S.S.P., et al., *Giant tunnelling magnetoresistance at room temperature with MgO (100) tunnel barriers.* Nature Materials, 2004. **3**(12): p. 862-867.

23. Bennett, P.A., et al., *Endotaxial Silicide Nanowires: A Review.* Thin Solid Films, 2011: p. (in press).

24. He, Z., et al., *Epitaxial titanium silicide islands and nanowires.* Surf. Sci., 2003. **524**(1-3): p. 148-56.

25. Stevens, M., et al., *Structure and orientation of epitaxial titanium silicide nanowires determined by electron microdiffraction.* J. Appl. Phys., 2003. **93**(9): p. 5670-4.

26. Hsu, H.C., et al., *Growth of high-density titanium silicide nanowires in a single direction on a silicon surface.* Nano Letters, 2007. **7**(4): p. 885-889.

27. Wang, D. and Z.Q. Zou, *Formation of manganese silicide nanowires on Si(111) surfaces by the reactive epitaxy method.* Nanotechnology, 2009. **20**(27): p. 275607-12.

28. Chen, S.Y., H.C. Chen, and L.J. Chen, *Self-assembled endotaxial alpha-FeSi2 nanowires with length tunability mediated by a thin nitride layer on (001)Si.* Applied Physics Letters, 2006. **88**(19): p. 193114-7.

29. Liang, S., et al., *Magnetic Iron Silicide Nanowires on Si(110).* Appl. Phys. Lett., 2006. **88**: p. 113111-4.

30. Ohira, Y., et al., *Iron nanowire formation in Si(110).* Japanese Journal of Applied Physics, 2008. **47**(7): p. 6138-6141.

31. George, T. and R.W. Fathauer, *Endotaxial Growth of Cosi2 within (111) Oriented Si in a Molecular-Beam Epitaxy System.* Applied Physics Letters, 1991. **59**(25): p. 3249-3251.

32. Bennett, P.A., et al., *In situ Observations of Endotaxial Growth of CoSi2 Nanowires on Si(110) using Ultrahigh Vacuum Transmission Electron Microscopy.* Nanotechnology, 2011: p. (in press).

33. Chen, S.Y. and L.J. Chen, *Nitride-mediated epitaxy of self-assembled NiSi2 nanowires on (001)Si.* Applied Physics Letters, 2005. **87**(25): p. 253111-3.

34. Cherns, D., et al., *Atomic structure of the NiSi2/(111)Si Interface.* Phil. Mag., 1982. **A46**(5): p. 849-862.

35. He, Z., D.J. Smith, and P.A. Bennett, *Epitaxial DySi2 nanowire formation on stepped Si(111).* Appl. Phys. Lett., 2005. **86**: p. 143110-3.

36. He, Z., et al., *Dysprosium Silicide Nanowires on Si(110).* Appl. Phys. Lett., 2003. **83**(25): p. 5292-94.

37. Lim, D.K., et al., *Structure and electronic properties of self-assembled Pt silicide nanowires on Si(100).* Nanotechnology, 2007. **18**(9): p. 95706-10.

38. Visikovskiy, A., M. Yoshimura, and K. Ueda, *Pt-induced structures on Si(110) studied by STM.* Applied Surface Science, 2008. **254**(23): p. 7626-7629.

39. Visikovskiy, A., M. Yoshimura, and K. Ueda, *Initial Stages of Platinum Silicide Formation on Si(110) Studied by Scanning Tunneling Microscopy.* Japanese Journal of Applied Physics, 2009. **48**(8): p. -.

40. Ye, G.F., M.A. Crimp, and J. Nogami, *Self-assembled Gd silicide nanostructures grown on Si(001).* Journal of Applied Physics, 2009. **105**(10): p. 33104-8.

41. McChesney, J.L., et al., *Gd disilicide nanowires attached to Si(111) steps.* Nanotechnology, 2002. **13**: p. 545.

42. Hasegawa, Y., I.W. Lyo, and P. Avouris, *Measurement of surface state conductance using STM point contacts.* Surf. Sci., 1996. **357-58**: p. 32-7.

43. Okino, H., et al., *In Situ Resistance Measurement of Epitaxial Silicide Nanowires.* App. Phys. Lett., 2005. **86**: p. 233108.

44. Yoshimoto, S., S. Hasegawa, and etc, *Four-point probe resistance measurements using PtIr-coated carbon nanotube tips.* Nano Letters, 2007. **7**: p. 956-9.

45. Kitaoka, Y., et al., *Direct detection of grain boundary scattering in damascene Cu wires by nanoscale four-point probe resistance measurements.* Applied Physics Letters, 2009. **95**(5): p. 052110.

46. www.rhk-tech.com.

47. gwyddion.net.

48. Albrektsen, O.S., H. W. M. ; Morch, K. A. ; Thoren, A. R. , *Reliable tip preparation for high-resolution scanning tunneling microscopy.* J. Vac. Sci. & Technol. B, 1994. **12**(6): p. 3187-3189.

49. Fink, H.-W., *Mono-atomic tips for scanning tunneling microscopy.* IBM J. Res. Develop., 1986. **30**(5).

50. Melmed, A.J., *THE ART AND SCIENCE AND OTHER ASPECTS OF MAKING SHARP TIPS.* Journal of Vacuum Science & Technology B, 1991. **9**(2): p. 601-608.

51. Mayer, T.M., D.P. Adams, and B.M. Marder, *Field emission characteristics of the scanning tunneling microscope for nanolithography.* Journal of Vacuum Science & Technology B, 1996. **14**(4): p. 2438-2444.

52. Rubio, G., N. Agrait, and S. Vieira, Phys. Rev. Lett., 1996. **76**.

53. Untiedt, C., et al., *Formation of a Metallic Contact: Jump to Contact Revisited.* Physical Review Letters, 2007. **98**(20).

54. Saenz, J.J. and R. Garcia, *Near field emission scanning tunneling microscopy.* App. Phys. Lett., 1994. **65**(23).

55. Russell, A.M., *Electron Trajectories in a Field Emission Microscope.* Jour Appl Physics, 1962. **33**(3).

56. Fowler, R.H. and L. Nordheil, *Electron emission in intense electric fields.* Proceedings of the Royal Society of London Series a-Containing Papers of a Mathematical and Physical Character, 1928. **119**: p. 173-181.

57. Young, R., J. Ward, and F. Scire, *Topographiner - Instrument for measuring surface microtopography.* Review of Scientific Instruments, 1972. **43**.

58. Fink, H.W., *Point-Source for Ions and Electrons.* Physica Scripta, 1988. **38**: p. 260-263.

59. Kirk, T.L., U. Ramsperger, and D. Pescia, *Near field emission scanning electron microscopy.* Journal of Vacuum Science & Technology B, 2009. **27**(1): p. 152-155.

60. Frolov, V.D., et al., *Scanning tunnelling microscopy: application to field electron emission studies.* Journal of Physics D-Applied Physics, 1999. **32**(7): p. 815-819.

61. Niedermann, P., *APPLICATION OF A SCANNING TUNNELING MICROSCOPE TO FIELD-EMISSION STUDIES.* Ieee Transactions on Electrical Insulation, 1989. **24**(6): p. 905-910.

62. Lim, D.K., et al., *Low resistivity of Pt silicide nanowires measured using double-scanning-probe tunneling microscope.* Applied Physics Letters, 2008. **92**(20): p. 203114.

63. Kavanagh, K.L., M.C. Reuter, and R.M. Tromp, *High-temperature epitaxy of Pt/Si(001).* J. Cryst. Growth, 1997. **173**: p. 393-401.

64. Liu, Z.X., et al., *A thin-film solar cell of high-quality beta-FeSi2/Si heterojunction prepared by sputtering.* Solar Energy Materials and Solar Cells, 2006. **90**(3): p. 276-282.

65. Lefki, K., et al., *OPTICAL AND ELECTRICAL CHARACTERIZATION OF BETA-FESI2 EPITAXIAL THIN-FILMS ON SILICON SUBSTRATES.* Journal of Applied Physics, 1991. **69**(1): p. 352-357.

66. Moroni, E.G., et al., *Cohesive, structural, and electronic properties of Fe-Si compounds.* Physical Review B, 1999. **59**(20): p. 12860-12871.

67. Paschen, S., et al., *Low-temperature transport, thermodynamic, and optical properties of FeSi.* Physical Review B, 1997. **56**(20): p. 12916-12930.

68. Herfort, J., H.P. Schonherr, and K.H. Ploog, *Epitaxial growth of Fe3Si/GaAs(001) hybrid structures.* Applied Physics Letters, 2003. **83**(19): p. 3912-3914.

69. Derrien, J., et al., *SILICIDE EPILAYERS - RECENT DEVELOPMENTS AND PROSPECTS FOR A SI-COMPATIBLE TECHNOLOGY.* Applied Surface Science, 1993. **70-1**: p. 546-558.

70. Derrien, J., et al., *SYNTHESIS AND PROPERTIES OF EPITAXIAL SEMICONDUCTING SILICIDES.* Applied Surface Science, 1993. **73**: p. 90-101.

71. Pronin, II, et al., *Magnetic ordering of the Fe/Si interface and its initial formation.* Journal of Applied Physics, 2008. **104**(10).

72. Mantl, S., *ION-BEAM SYNTHESIS OF EPITAXIAL SILICIDES - FABRICATION, CHARACTERIZATION AND APPLICATIONS.* Materials Science Reports, 1992. **8**(1-2): p. 1-95.

73. Schmitt, A.L., et al., *Synthesis and properties of single-crystal FeSi nanowires.* Nano Letters, 2006. **6**(8): p. 1617-1621.

74. Schmitt, A.L., et al., *Synthesis and applications of metal silicide nanowires.* Journal of Materials Chemistry, 2010. **20**(2): p. 223-235.

75. Seo, K., et al., *Diffusion-Driven Crystal Structure Transformation: Synthesis of Heusler Alloy Fe3Si Nanowires.* Nano Letters, 2010. **10**(9): p. 3643-3647.

76. Liang, S.D. and B.A. Ashcroft, *Electrical characterization of epitaxial FeSi2 nanowire on Si (110) by conductive-atomic force microscopy.* Journal of Materials Research, 2010. **25**(2): p. 213-218.

77. Liang, S., et al., *Phase Transformation in FeSi2 Nanowires.* J. Cryst. Growth, 2006. **295**: p. 166-71.

78. Kyllesbech-Larsen, K., et al., *Electric and magnetic transport in ion-beam sythesized a-FeSi2.* Mar. Res. Symp. Proc., 1993. **320**: p. 121.

79. Kim, T. and J.P. Bird, *Electrical signatures of ferromagnetism in epitaxial FeSi2 nanowires.* Applied Physics Letters, 2010. **97**(26).

80. Sidorenko, F.A., et al., *INVESTIGATION OF MULTIPARTICLE ATOMIC CORRELATIONS IN ALPHA-FE1-XSI2 BY MOSSBAUER-SPECTROSCOPY.* Journal of Physics and Chemistry of Solids, 1982. **43**(3): p. 297-303.

81. Aprilesi, G., et al., *ELECTRICAL TRANSPORT-PROPERTIES IN CO-SILICIDES FORMED BY THIN-FILM REACTIONS.* Journal of Applied Physics, 1986. **60**(1): p. 310-317.

82. Fan, H.J., U. Gosele, and M. Zacharias, *Formation of nanotubes and hollow nanoparticles based on Kirkendall and diffusion processes: A review.* Small, 2007. **3**(10): p. 1660-1671.

83. Julies, B.A., et al., *A study of the NiSi to NiSi2 transition in the Ni-Si binary system.* Thin Solid Films, 1999. **347**(1-2): p. 201-207.

84. Wawro, A., et al., *Thermal reaction of iron with a Si(111) vicinal surface: Surface ordering and growth of CsCl-type iron silicide.* Physical Review B, 2003. **67**(19).

85. vonKanel, H., et al., *Structural properties of epitaxial silicide layers on Si.* Applied Surface Science, 1996. **104**: p. 204-212.

86. von Kaenel, H., et al., *New epitaxially stabilized CoSi phase with the CsCl structure.* Phys. Rev. Lett., 1995. **74**(7): p. 1163-1166.

87. Wu, Y., et al., *Single-crystal metallic nanowires and metal/semiconductor nanowire heterostructures.* Nature, 2004. **430**: p. 61-5.

88. Meyer, B., *Intrinsic properties of NiSi.* J. Alloys and Compounds, 1997. **262/63**: p. 235.

89. Okino, H., et al., *In situ resistance measurements of epitaxial cobalt silicide nanowires on Si(110).* Applied Physics Letters, 2005. **86**(23): p. 233108.

90. von Kaenel, H., *Growth and Characterization of Epitaxial Ni and Co Silicides.* Mat. Sci. Rep., 1992. **8**(5): p. 193-269.

91. Kubo, O., et al., *One-dimensional Schottky contact between ErSi2 nanowire and Si(100).* App. Phys. Lett., 2006. **88**: p. 233117pp3.

92. Duboz, J.Y., et al., *Epitaxial Erbium silicide films on Si(111) surface.* Appl. Surf. Sci., 1989. **38**: p. 171-7.

93. Kubo, O., et al., *Epitaxially grown WOx nanorod probes for sub-100 nm multiple-scanning-probe measurement*, App. Phys. Lett., 2006. **88**: p. 254101.

94. Ottaviani, G., K.N. Tu, and J.W. Mayer, Phys. Rev. B, 1981. **24**: p. 3354.

95. Natelson, D., et al., *Fabrication of extremely narrow metal wires.* App. Phys. Lett., 2000. **77**(13): p. 1991-3.